# Changing fluid chemistry during continuous shearing in cataclastic fault zones – a semiquantitative analysis based on cathodoluminescence, microprobe and stable isotope analysis

Stefan HAUSEGGER[1] & Walter KURZ[2][*]

[1] Graz University of Technology, Institute of Applied Geosciences, Member of NAWI Graz#,

Rechbauerstrasse 12, A-8010 GRAZ, Austria;

[2] University of Graz, Institute of Earth Sciences, Member of NAWI Graz#, Heinrichstrasse 26, A-8010 GRAZ, Austria;

[*] Corresponding author, walter.kurz@uni-graz.at

## Abstract

Brittle fault rock samples from carbonate shear zones along the Salzach-Ennstal-Mariazell-Puchberg fault system (SEMP) have been analysed using cathodoluminescence microscopy (CL), microprobe analysis and stable isotope composition. The combination of these analytical methods provides an insight into comminution processes and fluid chemistry. The reconstruction of the evolution of fluid chemistry leads to a chronological classification of five fluid phases with respect to fluid chemistry, CL behavior and related structural processes. Initial cataclasis is accompanied by dedolomitization processes along crystal borders and intragranular fractures (Phase P1). Subsequent fluid precipitation phases (P2-P5) are characterized by variable Fe- (and Si-content) and therefore variable CL behavior.

Microprobe element mappings support the discrimination of Fe-bearing, non luminescent phases and Ca- and Mn- bearing fluids with bright luminescent calcite precipitations. Fe-bearing carbonates and Fe-hydroxide precipitation indicates fluid circulation in deeper parts of the stratigraphic sequence. These fluids are assumed to be derived from underlying clastic sequences of the Werfen Formation. Stable isotope signatures ($\delta^{13}C$ and $\delta^{18}O$) indicate mainly meteoric origin of penetrating fluids and variable amounts of fluids in the fault zone.


Kataklastische Störungsgesteine aus karbonatischen Störungszonen entlang des Salzach-Ennstal-Mariazell-Puchberg Störungssystems (SEMP) wurden mittels Kathodolumineszenzmikroskopie (CL), Elektronenstrahl-Mikrosondenanalyse and Massenspektrometrie für stabile Isotope untersucht. Die Kombination dieser Analysemethoden erlaubt eine detaillierte Analyse der Prozesse der Deformation und der dabei beteiligten Fluide. Die chemische Analyse der aus fluiden Phasen ausgefällten Zemente erlaubt eine chronologische Klassifikation in fünf Entwicklungsstufen bezüglich Fluidzusammensetzung, CL- Mikrostrukturen der ausgefällten Zemente, und den entsprechenden strukturellen Prozessen. Beginnende Kataklase wird von Dedolomitisierung entlang einzelner Kristalloberflächen und intragranularer Brüche begleitet (Phase P1). Nachfolgende Entwicklungsstufen (P2 bis P5) sind durch unterschiedlichen Fe- (und Si-) Gehalt der Fluide, und in weiterer Folge durch entsprechend variierende CL- Mikrostrukturen gekenzeichnet.

Elementverteilungsmuster bestätigen die Diskriminierung von Fe- führenden, nicht lumineszierenden Phasen von Ca- und Mg-hältigen, lumineszierenden Zementfällungen. Fe- führende Karbonate und Fe- Hydroxidfällungen weisen auf die Zirkulation von Fluiden durch tiefer liegende Formationen hin, und auf eine Wechselwirkung dieser Fluide mit klastischen Sequenzen der Werfen Formation. Signaturen stabiler Isotope ($\delta^{13}C$ and $\delta^{18}O$) zeigen, dass die wässrigen Lösungen hauptsächlich meteorischen Ursprungs sind, und dass die Fluidpenetration in die Störungszonen zeitlich variiert hat.

## 1. Introduction

The approach to investigate paleo-fluid flow and fluid chemistry in fault zones is variable since lithology of the host rock, deformation mechanisms (brittle, brittle/ductile, ductile) and the structural evolution of a fault zone are decisive for potential pathways for fluid flow (e.g. Marquer and Burkhard, 1992; Sample et al., 1993; Conti et al., 2001; Cello et al. 2001b; Abart et al. 2002; Bellot, 2007; Billi et al., 2007; Gabrielov et al., 2007; Fitz-Diaz et al., 2011). Besides structural analysis of fault zones and macroscopic investigations, micro-structural and geochemical analyses are essential for studies on fluid flow and fluid chemistry. Hence, our selection of analytical methods primarily comprises petrographic- and cathodoluminescence microscopy, stable isotope analysis, fluid inclusion analysis and determination of major and trace elements by variable analytical methods (e.g. Bustillo et al., 1992; Janssen et al., 1998; Caine and Foster, 1999; Cello et al., 2001; Cello et al., 2001b; Pili et al., 2002; Marfil et al., 2005; Micarelli et al., 2005; Barker Shaun et al., 2006; Hausegger et al., 2010).

This study is based the structural investigations and expends from results described by Hausegger and Kurz (2013) and comprises multiple analytical methods in order to obtain a semi-quantitative assessment on changing paleo-fluid chemistry in brittle carbonate shear zones during continuous shear. Microscopic analysis (petrographic microscopy and cathodoluminescence) are combined with microprobe analysis (backscattered electron images and element mappings) and stable

isotope analysis. Data from X-ray diffraction and ICP OES supported the interpretation of microscopic and geochemical data. This combination led to a chronological sequence of (1) changing paleo-fluid chemistry and (2) related deformation and fluid-rock interactions, respectively.

## 2. Geological setting

Investigated sites are located in the southernmost part of the Northern Calcareous Alps (Fig. 1). These Mesozoic units overly the Greywacke Zone (e.g., Mandl, 2000; Bauer, 1998; Schmid et al., 2004) which is characterized by a Palaeozoic volcanic-sedimentary sequence. The study sites are located within the Mürzalpen nappe which comprises Mesozoic cover sequences of Permian to Lower Triassic clastic terrigenous sediments at the base, overlain by massive platform carbonates (e.g., Mandl, 2000). The tectonic evolution of the Northern Calcareous Alps is characterized by multiple phases of nappe stacking from the Late Jurassic to the Early Cretaceous (e.g., Frisch and Gawlick, 2003), and Late Cretaceous shortening associated with tear fault- related pull apart basins (Wagreich and Decker, 2001).

Post-collisional lateral extrusion and eastward displacement of the southern parts of the NCA in the Late Oligocene to Middle Miocene generated E-W to NE-SW oriented sinistral strike-slip faults (Linzer et al., 1997; Wang and Neubauer, 1998; Frisch et al., 1998, 2000). This evolution can be sub-divided into several sub-events associated with the development of new fault planes and fault re-activation, and with variable principal stress orientations at a regional as well as a local scale. A sequence of the evolution of fault zones and the related deformation structures and stress orientation within the NCA was elaborated by e.g. Decker et al. (1994), Linzer et al. (1995, 1997, 2002), Decker and Peresson (1996), Peresson and Decker (1997), and Ortner (2003).

Conjugated strike-slip fault sets and (N)NE-directed reverse faults characterize a first deformation stage (D3 after Decker, 2002). Subsequent transtensional deformation events (D4 and D5 after Decker, 2002) are mainly characterized by re-activation of pre-existing fault planes. E-W compression in post Middle Miocene times regionally reactivated prior established fault systems (Decker et al., 1994; Decker and Peresson, 1996; Linzer et al., 1997; Peresson and Decker, 1997).

The most distinct structural feature in the Eastern Alps is the sinistral Oligocene-Miocene Salzach-Ennstal-Mariazell-Puchberg [SEMP] fault system (e.g. Ratschbacher et al., 1991; Decker et al., 1993; Decker and Peresson, 1996; Wang and Neubauer, 1998; Frisch et al., 2000; Schmid et al., 2004;). The fault system extends over 400 km from the Northern margin
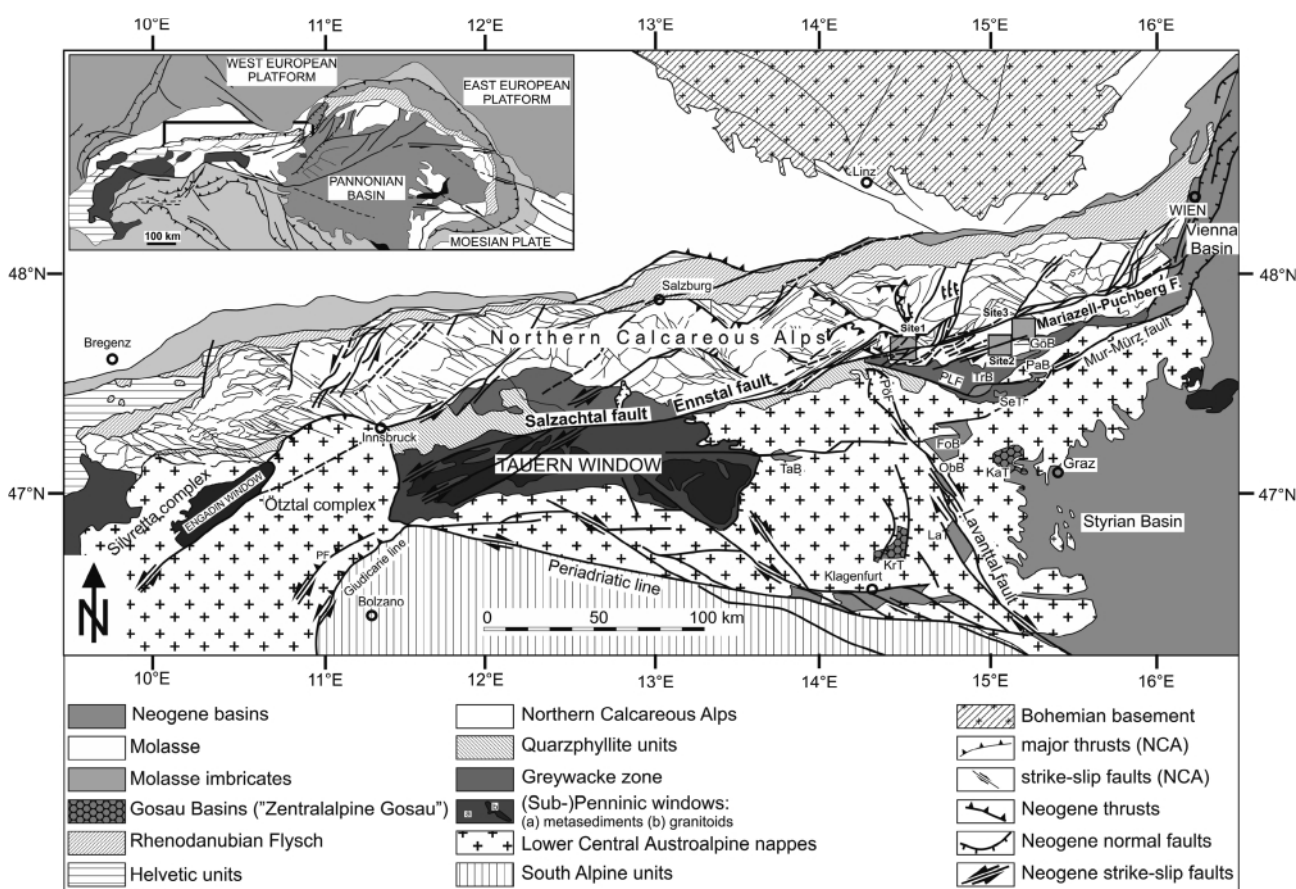


**Figure 1:** Tectonic map of the Eastern Alps displaying the Paleogene to Neogene fault system (after Linzer et al. 2002). The sites discussed in this contribution (see marked areas) are located along the Salzach-Ennstal-Mariazell-Puchberg fault (SEMP) (see Fig. 2). PF=Peijo fault; PLF =Palten – Liesing fault; PöF=Pöls fault; GöB=Göriach basin; PaB=Parschlug basin; SeB=Seegraben basin; FoB=Fohnsdorf basin; ObB=Obdach basin; TaB=Tamsweg Basin; TrB=Trofaiach Basin; LaT=Lavanttal Basin; KaT=Kainach Gosau Basin; KrT=Krappfeld Gosau Basin.

of the Tauern Window to the Vienna Basin (Fig. 1) and shows a maximum displacement of up to 60 km (Linzer et al., 1997, 2002). The central and eastern parts of the SEMP fault system exhibit brittle deformation over a broad segmented shear zone (Frisch et al., 2000; ; Linzer et al., 2002; Hausegger et al., 2010) that is mainly localized along the southern margin of the NCA. In addition to this major fault zone numerous sub-parallel E-W to NE-SW striking faults developed simultaneously, also within the NCA.

## 3. Site description

This study focuses on three different sites in the Ladinian Wetterstein-limestone/ -dolomite units of the Mürzalpen nappe (Fig. 1, 2). At the studied sites the northern margin of the Mürzalpen nappe is transsected by the SEMP fault system (Fig. 1). The sites are characterized by fault zones subparallel to the main SEMP fault system as well as conjugate faults with va-

rious orientations and displacements (Hausegger and Kurz, 2013). Site Haindlkar is located in the Gesäuse Mountains and directly affected by the Ennstal/Gesäuse fault, a segment of the SEMP fault system. Brandwald and Fölz represent the eastern part of the study area on the southern side of the Hochschwab massif (Fig. 1, 2).

### 3.1 Structural evolution

Nomenclature of structural elements follows common classifications (following e.g. Caine et al., 1996; Caine and Foster, 1999; Billi et al., 2003; Kim et al., 2004; Faulkner et al., 2010) and discriminates between host rock, damage zone, transition zone and fault core. Fault type classification and particle analysis were adopted from Hausegger and Kurz (2013), who describe a continuous fault zone evolution due to increasing displacement from initial fault type III over fault type II to mature fault type I (Fig. 3).
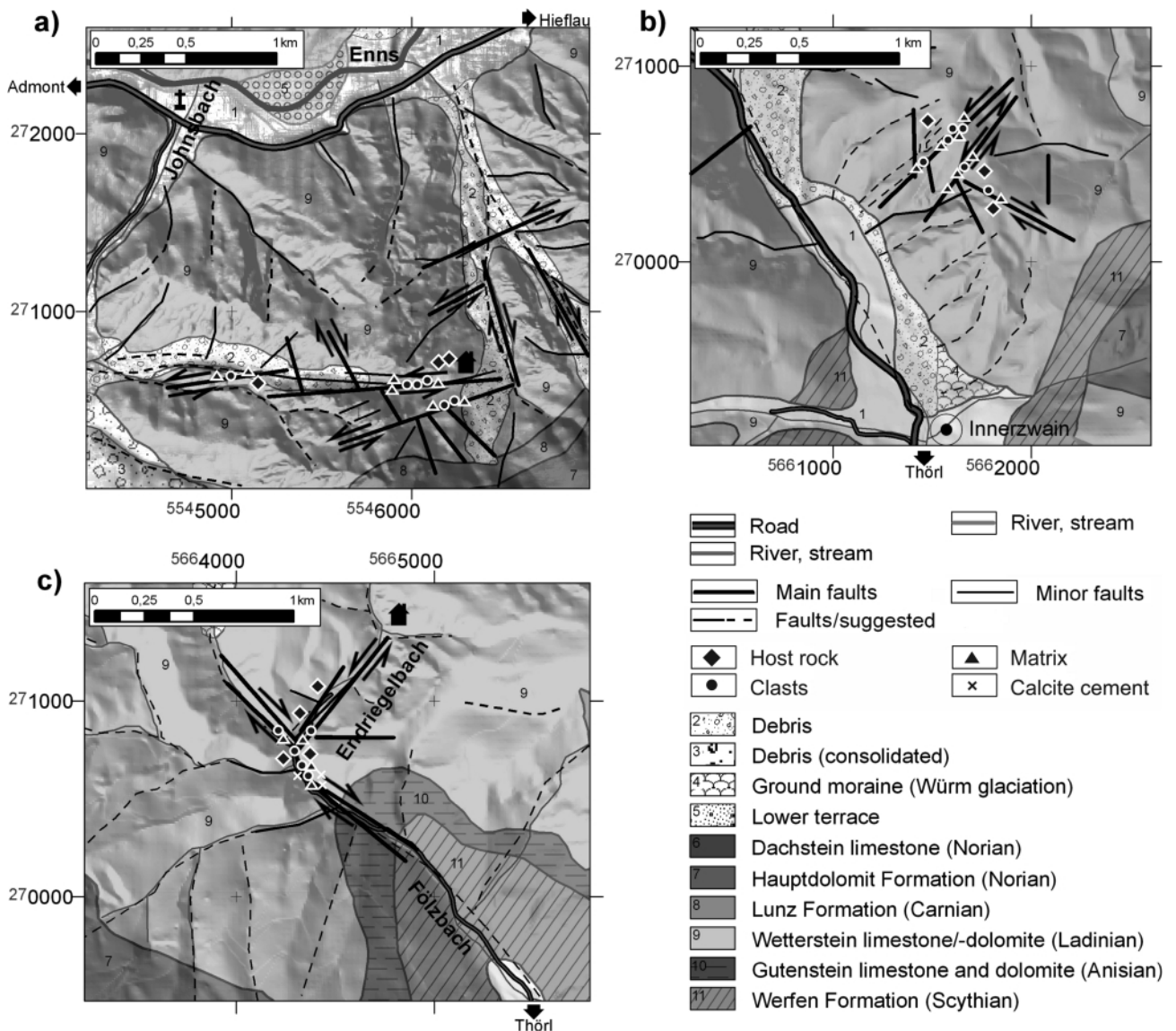


**Figure 2:** Digital Terrain Model (DTM) with overlaying geological map and sample locations of (a) site Haindlkar, (b) site Brandwald and (c) site Fölz (modified after Hausegger and Kurz 2013). Indication of sample locations (Tab.1) is sub-divided in „host rock", „clasts", „matrix" and „cement"-samples. Only fault zones that were identified in the field are displayed.
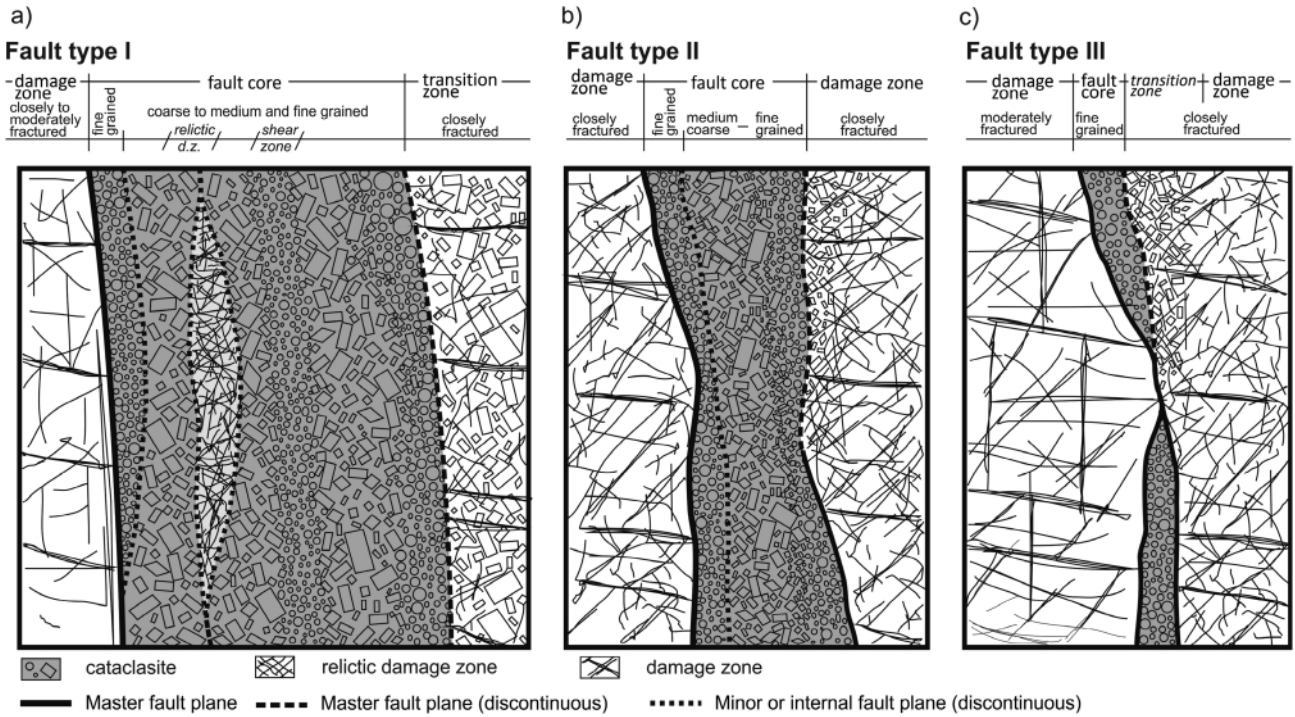
**FIGURE 3:** Conceptual cross sections of classified fault types (modified after Hausegger and Kurz 2013). (a) Fault type I (exclusively in main fault orientation and suitable thickness of more than 1m) is characterized by a complex internal fault core structure, composed of several domains of cataclasites, host rock lenses and internal fault planes (slickensides). (b) Fault type II shows an advanced state of fault core segmentation (shear bands and internal fault planes/slickensides) and thickness from 20 to 100 cm. (c) Fault type III is classified as uniform and solitary cataclasite layer with thicknesses less than 20 cm. All fault core cataclasites are composed of comminuted fragments (clasts) in a very fine-grained matrix of pulverized host rock (dolomite) and variable amount of secondary calcite.
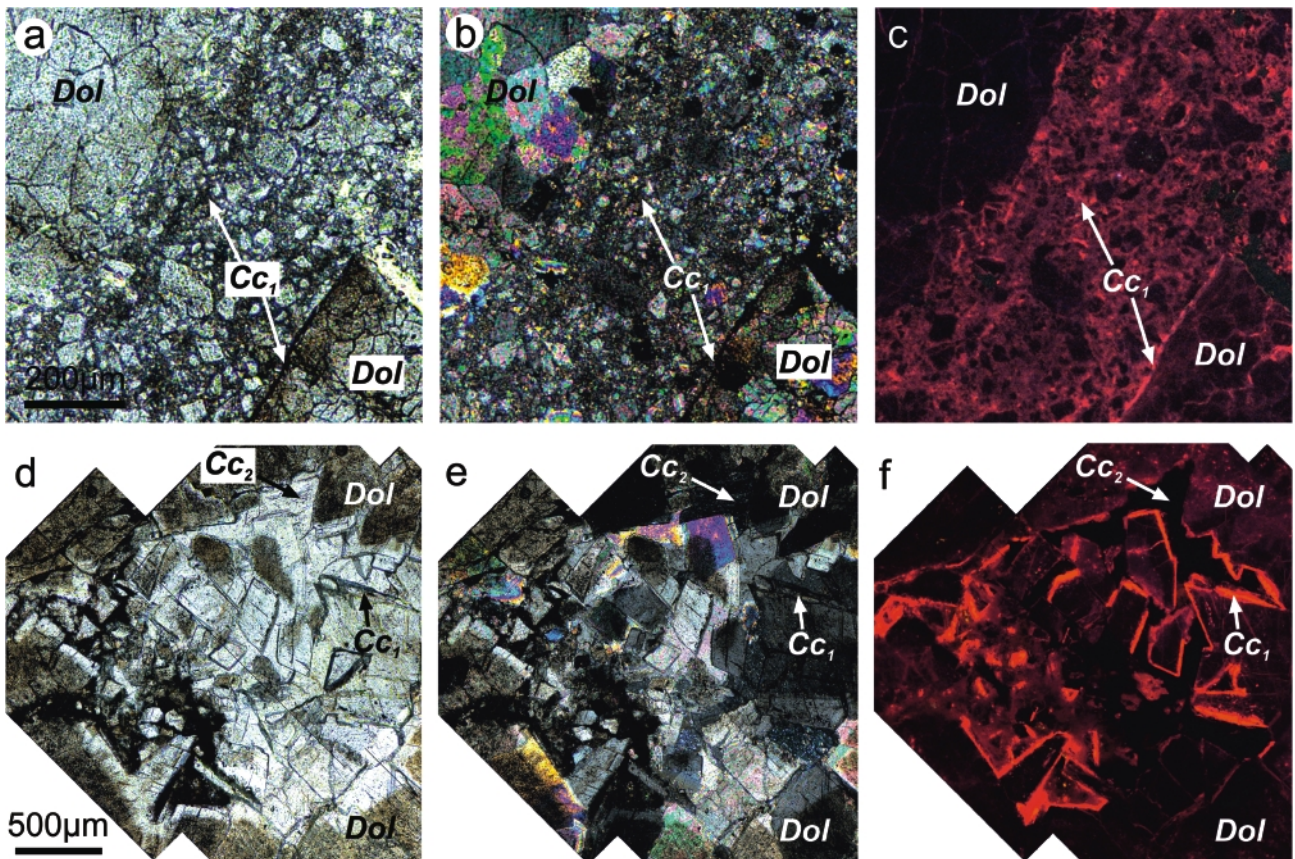


**FIGURE 4:** (a) Plane-light, (b) cross-polarized light and (c) CL image of a dolomite fault core cataclasite from site Haindlkar (sample G7). (d) Plane-light, (e) cross-polarized light and (f) CL image of a damage zone rock sample from site Haindlkar (sample H4). Parent rock material is dolomite ('Dol') with secondary calcite fillings and dedolomitizised crystal rims and matrix material ('$Cc_1$').
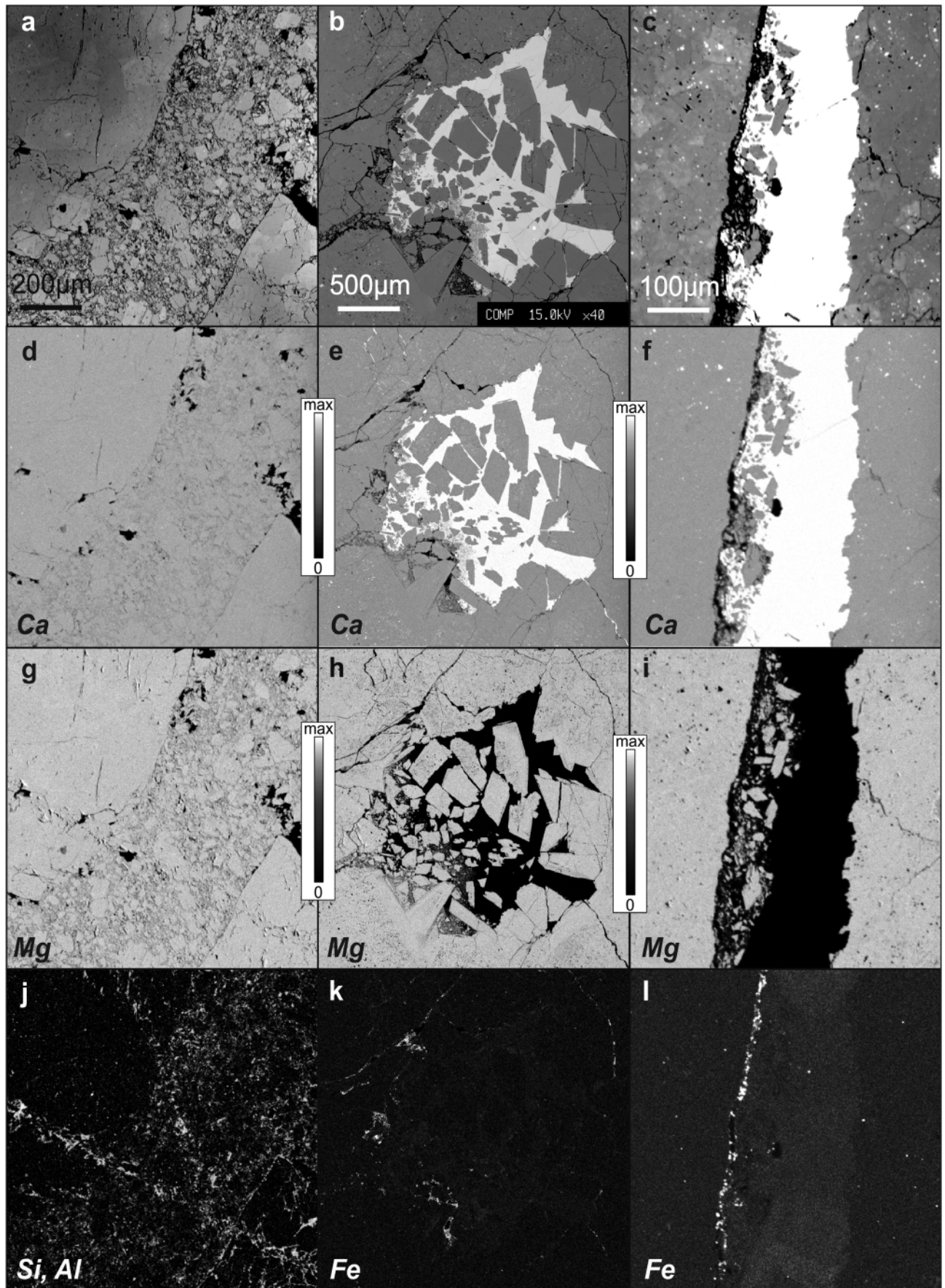
**FIGURE 5:** BSE image of (a) fault core cataclasite (sample G7), (b) damage zone (sample H4) and (c) detailed image of a damage zone calcite vein. In BSE images calcite is shown in bright grey to white and dolomite in dark grey colors. (d-f) Mapping of Ca content. (g-i) Mapping of Mg content. (j) Compiled element mapping of Si and Al of sample G7 (fault core cataclasite). (k, l) Fe mapping of sample H4 (damage zone) showing slightly increased Fe contents which quenches CL in areas of secondary calcite. All samples from site Haindlkar.

Fault type I is characterized by the most complex internal fault core structure. Several domains of cataclasites, distinct shear zones and relictic lenses of damage zone material are bordered by internal fault planes or gradual transition zones to adjacent domains. Cataclasite domains exhibit a wide range of particle size distributions, maximum particle size ($F_{max}$ from 2,5 to 13 mm) and matrix/clasts area ratios (matrix area from 55 to 90%). Type I fault cores reach widths of several 10's of meters (Fig. 3 a).

Fault type II represents an intermediate stage of development from fault type III (thin solitary cataclastic layers) towards fault type I. Type II fault cores are classified by an advanced internal segmentation of one to several shears and thicknesses up to 100 cm (Fig. 3 b). Fault core cataclasites show bulk proportion of matrix between 50 and 85% with a maximum clast diameter of 14 mm. Fault types I and II are configured in typical asymmetric cross sections. Fault cores are bordered by at least one master fault plane and, in some domains along strike, a variable transition zone towards the damage zone. Progressive fault development from Fault type III to Fault type II and Fault type I is limited to fault orientations that provide high or maximum shear stress ($\tau_{max}$) along the fault plane (Hausegger and Kurz, 2013). The thicknesses of fault cores, between planes of high to maximum shear stress concentration, reflect the main amount of displacement along the shear zone and mark the main fault orientation on each site. The investigated fault zone development proceeds according to Mohr-Coulomb fracture evolution described from Riedel type experimental configurations. The evolution of these cataclastic fault cores is depending on orientation with respect to principal stress axis as wellas pre-existing and predominant structures (Hausegger and Kurz, 2013).

## 4. Methodology and sample preparation

Coincidentally to field data acquisition and structural analysis (Hausegger and Kurz, 2013), oriented samples from all structural elements (host rock, damage zone and fault core) of fault zones were taken at the study sites described above (Fig. 2). Cubes of hand samples with an average edge length of 10 to 15 centimeters were cut out with a power saw in order to get sufficient sample size without destruction by hammer stroke or a drilling bit. Where possible, fault core and damage zone domains were sampled within one cube; otherwise, the distinct domains were sampled separately along strike. In-cohesive and highly fractured specimens were stabilized with synthetic resin. All samples were saw-cut into several sections with respect to the orientation of the related fault zone, i.e. perpendicular to the fault piane and parallel to the slickensides, coated with clear lacquer and scanned in high resolution (600dpi) using a CCD flatbed scanner for further image and particle analysis (Hausegger and Kurz, 2013). Thin-sections for petrographic microscopy, as well as polished and carbon-coated thin sections for cathodoluminescence- and microprobe analysis were prepared at the University of Graz, Institute of Earth Sciences were.

Powder samples for stable isotope analysis were categorized as "host rock", "clasts" (cataclasite particles), "matrix" (mainly comminuted dolomite) and "calcite cement". In order to minimize cross contamitation of clasts and embedding material two different sampling methods were conducted. (1) In fine grained cataclasites (clasts less than 6 mm in diameter)clasts and matrix material have been seperated by hand using a steel needle under an illuminated magnifier and subsequently
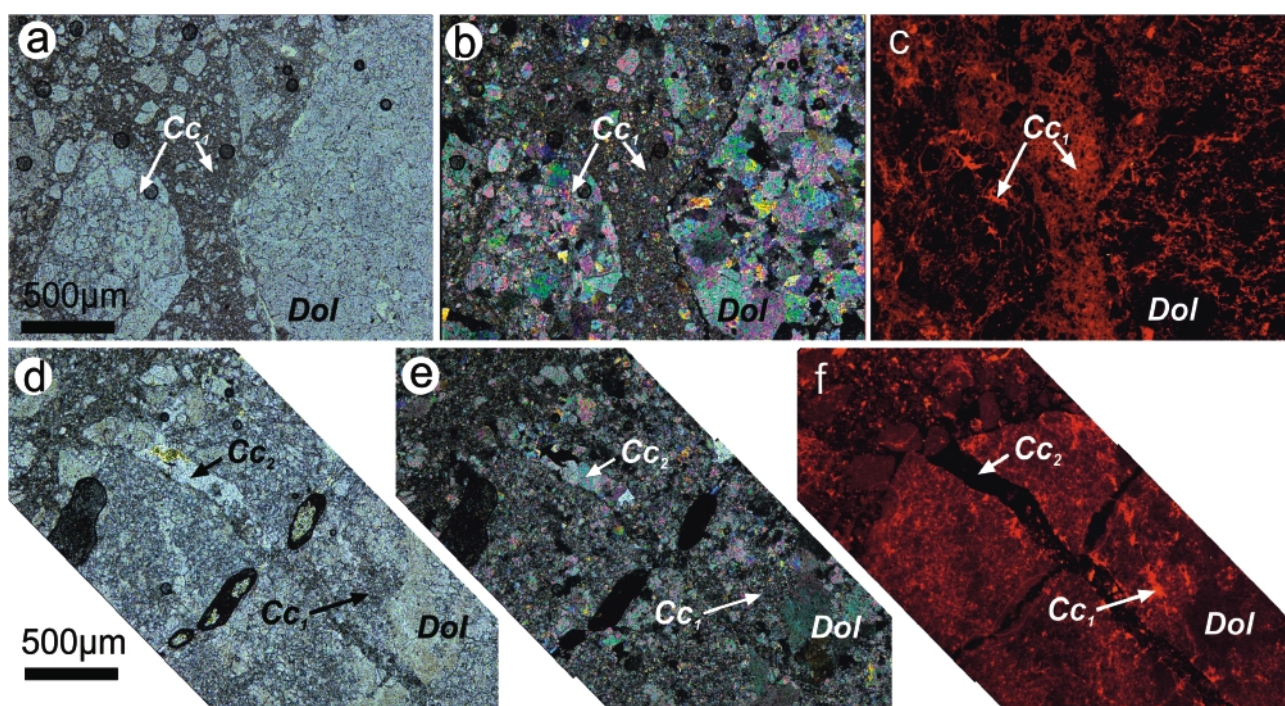


**Figure 6:** (a) Plane-light, (b) cross-polarized light and (c) CL image of a fault core cataclasite from site Brandwald (fault type II; sample B8). (d) Plane-light, (e) cross-polarized light and (c) CL image of the main fault core cataclasite from site Brandwald (fault type I; sample B11). Parent rock material is dolomite ('Dol') with secondary calcite fillings, dedolomitizised crystal rims and matrix material ('Cc₁') as well as subsequent calcite veins ('Cc2').
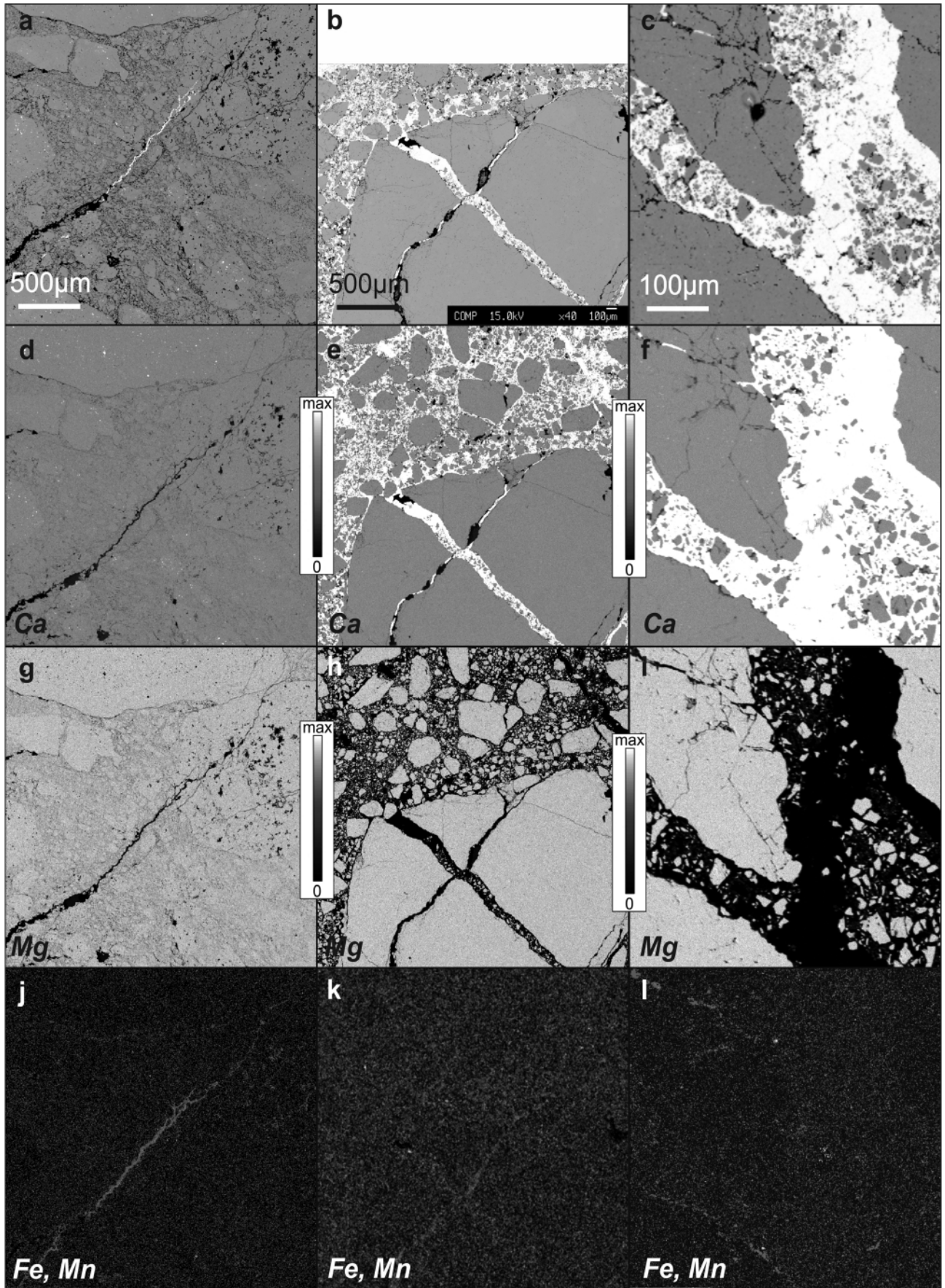
**Figure 7:** BSE image of (a) fault core cataclasite (fault type II; sample B8), (b) fault core cataclasite (fault type I; sample B11) and (c) detailed image of a calcite vein in fault type I cataclasites. Calcite and Fe-rich vein fillings (a) are shown in bright grey to white and dolomite in dark grey colors. (d-f) Mapping of Ca content. (g-i) Mapping of Mg content. (j-l) Compiled Fe-Mn mappings express areas of increased Fe-content (brighter areas and veins). All samples from site Brandwald.

pulverized in an agate mortar. (2) Powder samples of cataclasites with bigger clasts and sufficient matrix ratio were collected with a micro-drilling gear.

## 5. Results

### 5.1 Site Haindlkar

At this site, subhorizontally bedded Wetterstein limestone and dolomite (Ladinian) is trans sected by subvertical faults with a general (WS)W – (EN)E trend. These main faults show sinistral displacement and are associated with conjugate NNW – SSE striking dextral faults (Fig. 2). Fault core cataclasites from the major fault zone at site Haindlkar (fault type I) are composed of dolomite components embedded in a fine grained matrix of comminuted dolomite (Fig. 4 a, b). Cathodoluminescence analysis (Fig. 4 c) exhibits typical dull to dark red colors for dolomite components. Distinct bright red luminescence is visible along crystal borders and intra-granular fractures, respectively. Though the matrix material is dolomite, luminescence along crystal borders causes bright red luminescence of areas composed of fine grained matrix material.

Damage zone samples of minor faults, sub-parallel to the main fault direction (fault type II) are characterized by calcite veins and pore fillings in a dolomite host rock (Fig. 4 d-f). Analogue to fault core cataclasites (Fig. 4 a-c), the dolomite parent rock material shows dull red luminescence, whereas bright red colors are concentrated along crystal borders and intra-

granular fractures, respectively. Secondary calcite pore fillings offer no luminescence and stay dark (Fig. 4 f).

Microprobe analysis, BSE images as well as element mappings of described samples (Fig. 5) support the observations from optical microscopy and CL. The matrix of the fault core cataclasite (Fig. 4 a-c) consists of comminuted dolomite material derived from the parent rock (Fig. 5 a). Element mappings of Ca and Mg show a slight decrease of Mg along crystal borders and intra-granular fractures (Fig. 5 d, g). Subsequent to brittle deformation/comminution of dolomite host rock, continuous shear resulted in the development of a cataclastic shear zone (Fig. 5 a, d, g, j). The compiled map of Si and Al distribution (Fig. 5 j) underlines this feature and classifies this deformation band and matrix as area of increased Si content.

The parent rock material of the investigated damage zone shows similar composition of Ca and Mg with respect to the fault core cataclasite (Fig. 5 e, f, h, i). However, pore volumes and fractures are filled with secondary calcite with almost no Mg (Fig. 5 e, f). In element mappings of Fe (Fig. 5 k, l) a slight increase of Fe is visible in calcite fillings, which is responsible for quenched luminescence of these areas (Fig. 4 f).

### 5.2 Site Brandwald

At Brandwald, moderately southward dipping Wetterstein limestone and dolomite (Ladinian) is transsected by subvertical faults with a general SW – NE trend with sinistral sense of shear. These main faults are associated with conjugate NW–
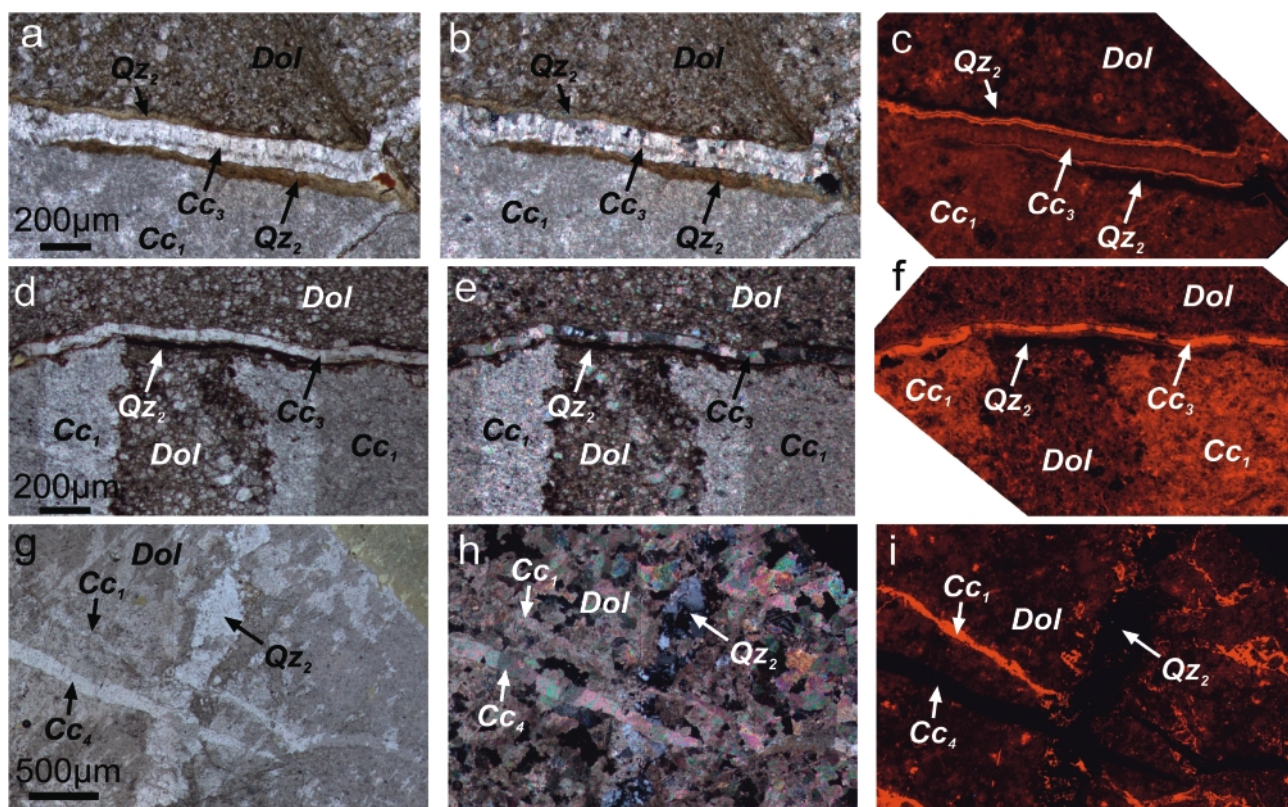


**Figure 8:** (a, d) Plane-light, (b, e) cross-polarized light and (c, f) CL image of an ultracataclasite from site Fölz (samples EA1, EA2). (g) Plane-light, (h) cross-polarized light and (i) CL image of a fault core cataclasite from site Fölz (sample R14). Parent rock material is dolomite ('Dol'). Dedolomitizised material and vein fillings ('$Cc_1$'), quartz filled veins ('$Qz_2$') and subsequent calcite veins ('$Cc_3$ and $Cc_4$') are distinguished.
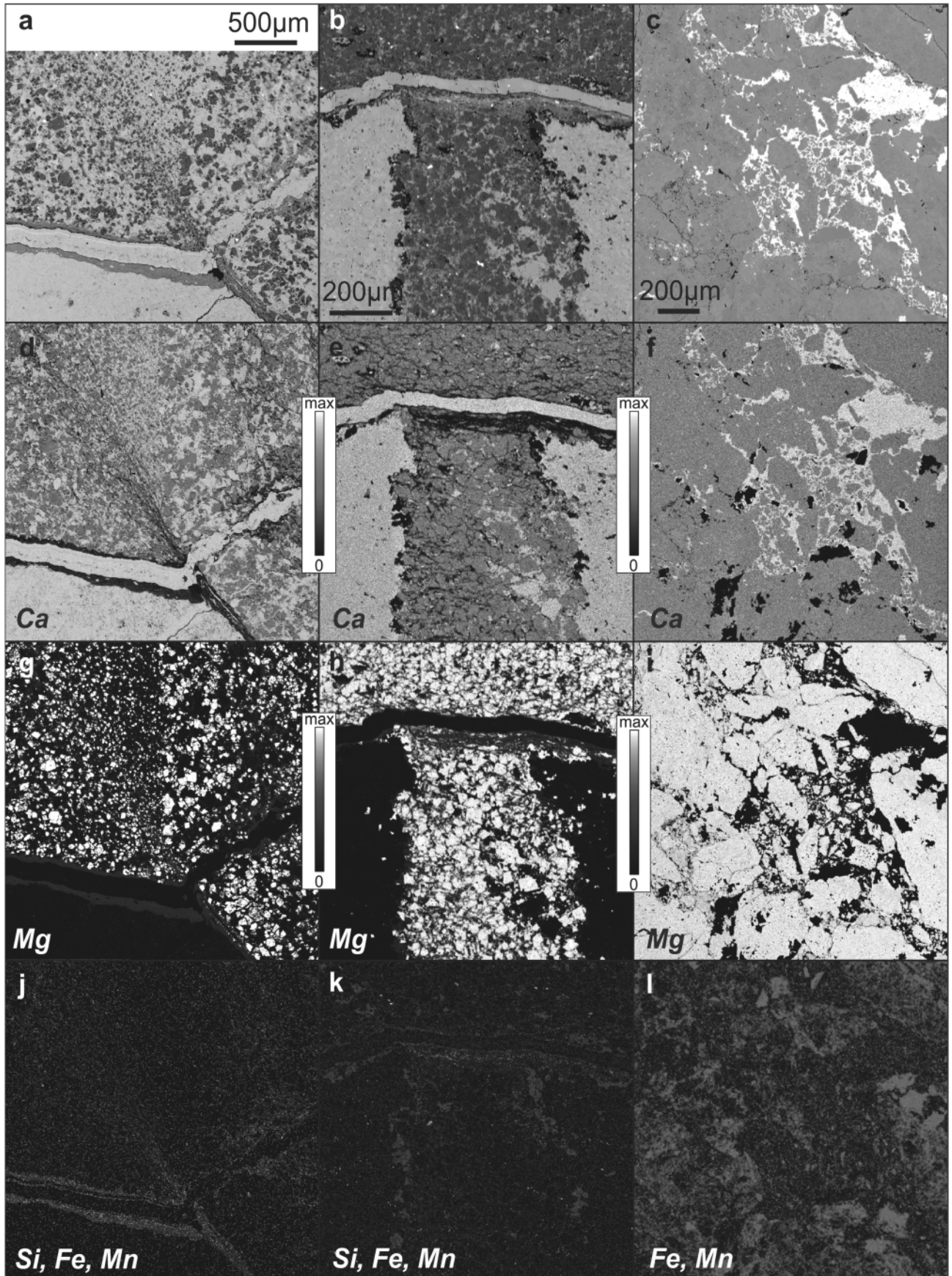
**Figure 9:** BSE image of (a, b) ultracataclasite (samples EA1 and EA2) and (c) fault core cataclasites (sample R14). Calcite (Ca) is shown in bright grey to white and dolomite (Mg) in dark grey colors. (d-f) Mapping of Ca content. (g-i) Mapping of Mg content. (j, k) Compiled element mapping of Si, Fe and Mn of ultracataclasite samples EA1 and EA2 showing constant Mn distribution (dark) and increased Fe- (gray) and Si- (bright grey) content in the outer rims of calcite filled veins and in intergranular pore volume. (l) Compiled Fe-Mn mapping of cataclasite sample R14. Mn shows constant distribution, whereas Fe content in calcite areas is very low. All samples from site Fölz.

SE and N –S striking dextral faults (Fig. 2). At this site samples from two different fault core cataclasites were analyzed. Minor fault type II cataclasites (Fig. 6 a-c) consist of dolomite components in a very fine grained dolomite matrix. Subsequent fractures and pore volumes are partly filled with secondary calcite and Fe-hydroxides. CL shows typical dark to dull red luminescence colors of dolomite components. As already described at site Haindlkar crystal borders and intra-granular fractures exhibit bright red luminescence. Hence, the matrix area, composed of very fine grained dolomite, appears like an almost continuous area of bright luminescence.

Fault core cataclasites from the main fault zone at site Brandwald (fault type I) also consist of dolomite components and comminuted, fine grained matrix material (Fig. 6 d, e). Additionally calcite cement and vein fillings are dominant in this sample (Fig. 6 d-f). In CL images (Fig. 6 f) dolomite components and matrix areas show dull red luminescence but appear slightly brighter than components in Fig. 6 c. Bright red luminescence is visible along crystal borders and intra-granular

fractures but also in irregular shaped areas inside dolomite components. Calcite cements and vein fillings stay dark under the bombardment of the hot cathode (Fig. 6 f).

Element mappings and BSE images of cataclasites from minor faults (Fig. 7 a, d, g, j) underline impressions from optical microscopy and CL. Components as well as comminuted matrix material mainly consist of dolomite. Element mappings of Ca and Mg support results from CL analysis and express a decrease of Mg along crystal borders and intra-granular fractures (Fig. 7 d, g). Compiled Fe-Mn mappings (Fig. 7 j) clearly indicate Fe-bearing (Fe-hydroxide) vein fillings in intra- and inter-granular fractures and crystal borders.

Derived from the same dolomite parent rock material, fault type I cataclasites can be distinguished by the presence of calcite cement and calcite vein fillings in intra-granular fractures (Fig. 7 b, c). Similar to minor faults (Fig. 7 a) a decrease in Mg is detected along crystal borders (Fig. 7 e, h, k) as well as Fe-rich crack fillings. However, Ca-(calcite) cement and vein fillings (Fig. 7 e, f) differ this cataclasite type from type II fault
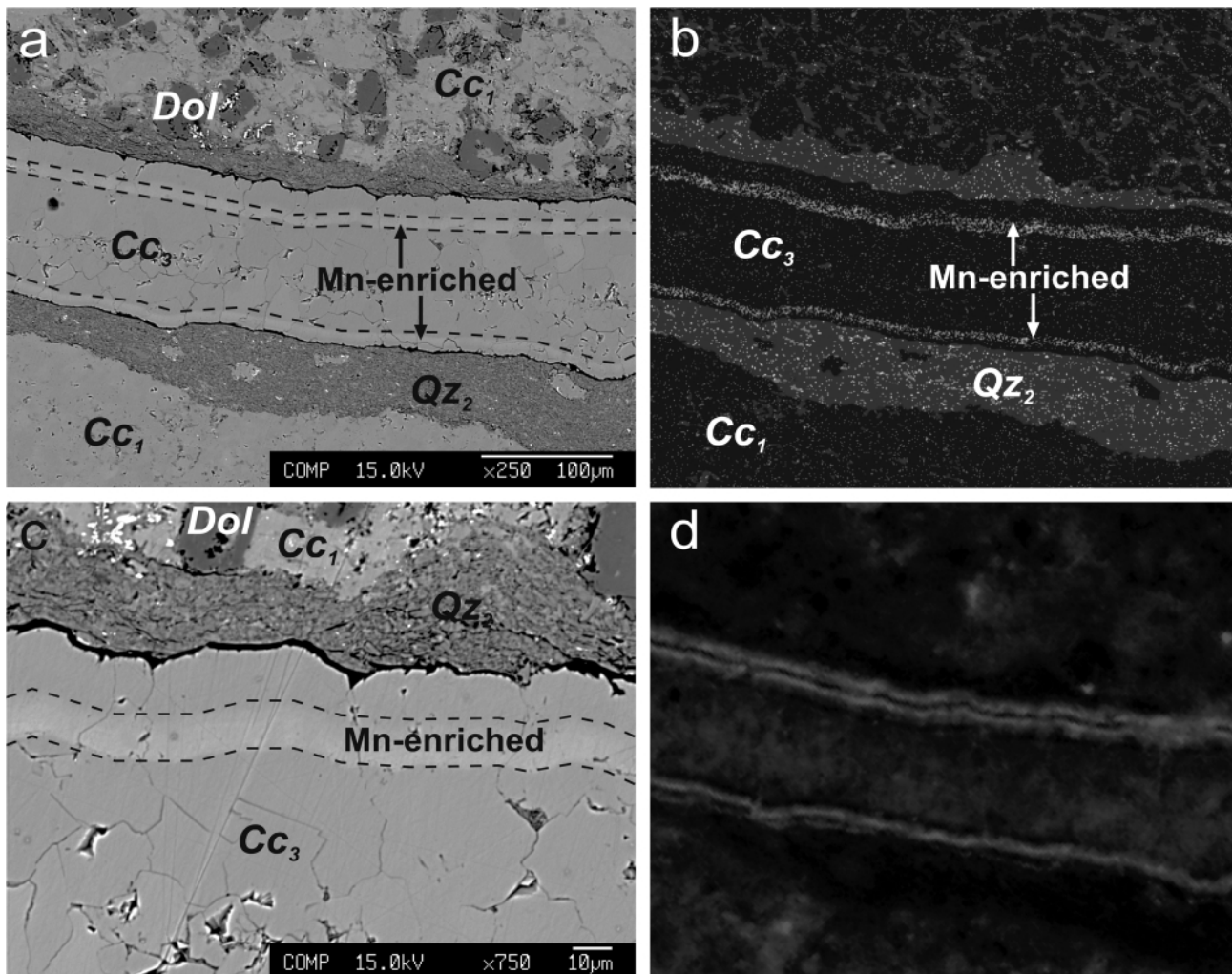


**Figure 10:** (a, c) BSE image of a secondary calcite vein in ultracataclasite sample EA1. Dolomite clasts ('Dol') are embedded in de-dolomitized material ('Cc$_1$'). Calcite vein Cc$_3$ strikes through former quartz veins ('Qz$_2$') and exhibits internal zonation, showing bands of increased Mn content. (b) Combined element mapping of Si, Mn and Fe illustrates Mn enriched bands and quartz precipitation in veins and intergranular pore space. (c) Detailed image of the upper rim of the calcite vein. (d) CL image clearly illustrates the bright luminescence of Mn-enriched bands. Dedolomite domains show darker luminescence colours. Quartz rich areas stay dark.

core samples in Fig. 7 a, d, g, j. Compiled Fe-Mn mappings exhibit slightly increased Fe-contents in areas of calcite cements and fillings (Fig. 7 k, l). This change in Fe-content is manifested in the missing luminescence of this calcite generation.

## 5.3 Site Fölz

Former structural analysis (Hausegger and Kurz, 2013) identified this site as fault zone with a complex structural evolution. NW – SE trending, subvertcal dextral fault zones crosscut Wetterstein limestone and dolomite, Gutenstein limestone and dolomite (Anisian) as well as the underlying Permian to Scythian clastic Werfen formation. Antithetic NE-SW trending strike-slip fauts are situated within Wetterstein limestone and dolomite (Fig. 2). Investigated fault cores from site Fölz consist of ultracataclasites (Fig. 8 a – f) and cataclasites (Fig 8 g-i), both derived from dolomite host rocks.

Ultracataclasites are built up by dolomite components, particle diameter from 10 to 50 μm, embedded in a fine grained calcite matrix (Fig. 8 a, b, d, e). Bands of dolomite components and calcite define a layered internal structure. Vein fillings show a distinct zonation of quartz along the rims and calcite inside the vein (Fig. 8 a-f). Quartz-rich areas stay dark in CL, whereas dolomite components exhibit typical dull red luminescence. Calcite, whether cement/matrix or vein fillings, glares in bright red colors. Furthermore, CL exposes an internal zonation of calcite vein fillings, represented by small bands of brighter luminescence towards quartz vein rims (Fig. 8 c).

Fault core cataclasites (Fig. 8 g-i) consist of dolomite components in a matrix of comminuted dolomite material and calcite cement in inter-granular pore volumes and intragranular fractures. Microscopy and CL images display different generations of quartz and calcite vein fillings (Fig. 8 g-i). In Cl images dolomite components stay dull red but calcite filled intra- and inter-granular volumes show bright red luminescence. Quartz filled as well as discordant calcite filled veins show no luminescence (Fig. 8 i).

BSE images and element mappings of Ca and Mg of ultraca-

taclasite samples (Fig. 9 a, b, d, e, g, h) show distinct areas of dolomite components embedded in calcite cement/matrix. Surrounded by calcite filled veins, areas of almost pure calcite matter without any dolomite components are visible in Fig. 9 a, d, g, h below the calcite vein and Fig. 9 b, e, h, k on the left and right image border below the calcite vein. Cataclasite fault core samples consist of dolomite components and mainly calcite cement and vein fillings (Fig. 9 c, f, i). Combined Fe-Mn element mappings show very low Fe contents in primary calcite cement and vein fillings. This lack of Fe-quenching is visible as bright red to orange luminescence (Fig. 8).

## 5.4 Deformation and precipitation phases

Distinct stages of deformation and cementation were defined chronologically with respect to the chemical composition of the precipitates and the related CL observations in a sequence of five phases (Fig 10, 11):

Phase 1 (P1) concerns all sites and analyzed samples. Dedolomitization, as described above, is visible in variable distinctness. This stage comprises dedolomitization processes synchronous and subsequent to cataclastic events. Chemistry of precipitated cement is characterized as Ca-rich with a very low amount of Fe and an adequate Mn content, indicated by bright red luminescence along crystal borders and intra-granular fractures (Fig. 4, 6, 8).

Phase 2 (P2) is subdivided with respect to cement chemistry in two different stages. At site Fölz quartz filled veins and cemented pores indicate precipitation from Si-rich fluid phases (Fig. 8). Samples from site Haindlkar and site Brandwald exhibit pores and veins cemented by euhedral to subhedral calcite assumed to have derived from Ca-rich fluids. The cements are characterized by an increased Fe content with respect to phase P1. Precipitation of Fe-hydroxides in veins and pores were distinguished in samples from site Brandwald and Fölz (Fig. 7 j-l; 9 j, k). As a basic principle increased Fe-content quenches luminescence. Therefore, precipitated calcite from this phase can be easily distinguished from early dedolomiti-
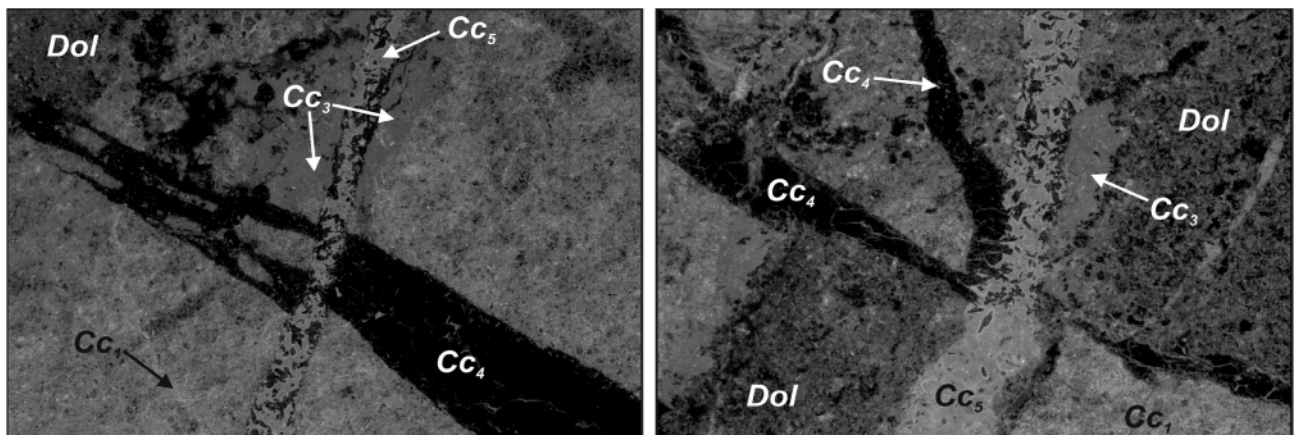


**Figure 11:** CL images of ultracataclasites from site Fölz (samples EA1 and EA2) illustrating CL behavior and chronological sequence of all five precipitation phases (phase P1 to P5). Calcite cement derived from de-dolomitization ('Cc$_1$') and phase P3 ('Cc$_3$') show intermediate to bright luminescence. Calcite veins from phase P4 ('Cc$_4$') with no luminescence developed sub-perpendicular to Cc$_3$-veins. Bright red calcite veins from phase P5 ('Cc$_5$') strike through dark Cc$_4$ veins, dragging non-luminescent material from phase P4 along the course of P5 veins.

zation features (Fig. 4 f; 5; 6 c, f; 7).

Phases 3 to 5 (P3-P5) exclusively developed at site Fölz. P3 is restricted to ultracataclasite samples and characterized by calcite vein fillings with bright red luminescence. These veins developed in concordant quartz veins from phase P2 (Fig. 8, 9) and show an internal zonation of Mn-bearing bands, visible as bright stripes in CL images (Fig. 10).

Phase 4 represents another change in cement chemistry and deformation. Calcite filled veins developed sub-perpendicular to no-luminescent quartz and calcite veins from phase P3 (Fig. 8 g-i, 11). Chemical composition (high Fe-amount and low Mn-values) prevents any luminescence of P4-vein fillings.

The latest stage of marks another change in cement chemistry. Phase 5 (P5) calcite veins crosscut all prior features and show a very bright red luminescence (Fig. 11).

## 5.5 Stable isotope analysis

At site Haindlkar host rock and cataclasite components show constant $\delta^{13}C$ values from 3.16 to 3.93 ‰ and variable $\delta^{18}O$ values (1.49 to -0.47 ‰) from host rock to cataclasite components. Cataclasite matrix/cement exhibits similar $\delta^{18}O$ values with respect to components but shows more variable $\delta^{13}C$ values from 1.86 to 3.38 ‰ (Fig. 12 a) (Tab. 1).

Stable isotope composition at site Brandwald shows similar patterns with respect to site Haindlkar. Host rock and cataclasite components plot in a field of uniform $\delta^{13}C$ values (2.90 to 3.74 ‰) and variable $\delta^{18}O$ values from -2.31 to 0.18 ‰. Cataclasite matrix/cement generally shows lower values for $\delta^{18}O$ than host rocks and clasts (-3.94 to -1.38 ‰). Similar to site Haindlkar, matrix/cement is more variable in $\delta^{13}C$ values and ranges

**Table 1:** Site and location of analyzed samples. Stable isotope data of host rock, cataclasite clasts, cataclasite matrix and secondary calcite cement samples.

| Site | Sample | Sample type | Sample locationS | | $\delta^{18}O$ | $\delta^{13}C$ |
|---|---|---|---|---|---|---|
| Haindlkar | G10 H1 | host rock | 47°34'01.97"N | 14°36'14.14"E | 1,07 | 3,93 |
| | G10 H2 | host rock | 47°34'01.97"N | 14°36'14.14"E | 0,95 | 3,80 |
| | G6 H1 | host rock | 47°34'01.74"N | 14°35'57.45"E | 1,49 | 3,47 |
| | G2 K | clasts | 47°34'01.49"N | 14°35'47.81"E | 0,08 | 3,41 |
| | G7 K1 | clasts | 47°34'01.22"N | 14°36'13.77"E | 1,21 | 3,48 |
| | G8 K | clasts | 47°34'01.22"N | 14°36'13.77"E | 0,66 | 3,57 |
| | G9 K | clasts | 47°34'01.22"N | 14°36'13.77"E | -0,47 | 3,48 |
| | H6 K1 | clasts | 47°33'56.60"N | 14°36'15.39"E | 0,65 | 3,16 |
| | H7 K1 | clasts | 47°33'56.37"N | 14°36'14.13"E | 0,50 | 3,45 |
| | G11 Z | matrix | 47°34'03.19"N | 14°36'15.26"E | -0,23 | 2,77 |
| | G12 Z | matrix | 47°34'03.19"N | 14°36'15.26"E | 0,29 | 3,36 |
| | G13 Z | matrix | 47°34'03.19"N | 14°36'15.26"E | -0,13 | 3,16 |
| | G2 Z | matrix | 47°34'01.49"N | 14°35'47.81"E | -1,32 | 1,86 |
| | G3 Z | matrix | 47°34'01.49"N | 14°35'47.81"E | 0,03 | 3,07 |
| | G5 Z | matrix | 47°34'01.33"N | 14°35'51.46"E | -0,19 | 3,36 |
| | G7 Z1 | matrix | 47°34'01.22"N | 14°36'13.77"E | -0,44 | 2,63 |
| | G9 Z1 | matrix | 47°34'01.22"N | 14°36'13.77"E | 0,38 | 3,25 |
| | H6 Z2 | matrix | 47°33'56.60"N | 14°36'15.39"E | 0,10 | 2,79 |
| | H7 Z1 | matrix | 47°33'56.37"N | 14°36'14.13"E | 0,68 | 3,28 |
| | H7 Z2 | matrix | 47°33'56.37"N | 14°36'14.13"E | 0,49 | 3,38 |
| Brandwald | B10 H1 | host rock | 47°33'55.58"N | 15° 9'12.72"E | -0,46 | 3,74 |
| | B6 K1 | host rock | 47°33'55.96"N | 15° 9'12.56"E | 0,09 | 3,54 |
| | B2 K1 | host rock | 47°33'55.46"N | 15° 9'14.92"E | 0,18 | 3,50 |
| | B8 H1 | clasts | 47°33'55.92"N | 15° 9'14.02"E | -2,31 | 3,40 |
| | B1 K1 | clasts | 47°33'55.15"N | 15° 9'15.45"E | -1,70 | 2,90 |
| | B1 K2 | clasts | 47°33'55.15"N | 15° 9'15.45"E | -1,12 | 3,21 |
| | B10 K1 | clasts | 47°33'55.58"N | 15° 9'12.72"E | -1,09 | 3,59 |
| | B11 K1 | clasts | 47°33'55.58"N | 15° 9'12.72"E | -1,14 | 3,44 |
| | B13 K1 | clasts | 47°33'55.58"N | 15° 9'12.72"E | -1,26 | 3,53 |
| | B19 K1 | clasts | 47°33'57.24"N | 15° 9'12.99"E | -0,29 | 3,50 |
| | B19 Z1 | matrix | 47°33'57.24"N | 15° 9'12.99"E | -3,86 | - |
| | B6 Z1 | matrix | 47°33'55.96"N | 15° 9'12.56"E | -2,42 | 3,11 |
| | B1 Z1 | matrix | 47°33'55.15"N | 15° 9'15.45"E | -3,94 | - |
| | B10 Z1 | matrix | 47°33'55.58"N | 15° 9'12.72"E | -3,17 | - |
| | B10 Z2 | matrix | 47°33'55.58"N | 15° 9'12.72"E | -3,83 | - |
| | B8 Z1 | matrix | 47°33'55.92"N | 15° 9'14.02"E | -2,31 | 3,40 |
| | B6 Z2 | matrix | 47°33'55.96"N | 15° 9'12.56"E | -1,72 | 3,18 |
| | B13 Z1 | matrix | 47°33'55.74"N | 15° 9'12.45"E | -2,09 | 0,32 |
| | B2 Z1 | matrix | 47°33'55.46"N | 15° 9'14.92"E | -1,45 | 2,10 |
| | B11 Z1 | matrix | 47°33'55.58"N | 15° 9'12.72"E | -1,96 | 0,60 |
| | B11 Z2 | matrix | 47°33'55.58"N | 15° 9'12.72"E | -1,83 | 1,83 |
| | B13 Z2 | matrix | 47°33'55.58"N | 15° 9'12.72"E | -1,38 | 1,33 |
| | B2 Z1 | matrix | 47°33'55.46"N | 15° 9'14.92"E | -3,62 | 0,94 |
| Fölz | R18 H1 | host rock | 47°34'10.52"N | 15°11'36.03"E | -2,38 | 3,29 |
| | R18 H2 | host rock | 47°34'10.52"N | 15°11'36.03"E | -1,34 | 3,10 |
| | R10 H1 | host rock | 47°34'11.03"N | 15°11'35.81"E | -1,76 | 3,27 |
| | R9 H1 | host rock | 47°34'11.16"N | 15°11'35.91"E | -1,40 | 3,73 |
| | R9 H2 | host rock | 47°34'11.16"N | 15°11'35.91"E | -1,31 | 3,86 |
| | R19 K1.6 | host rock | 47°34'10.09"N | 15°11'36.07"E | -1,56 | 3,69 |
| | R12 K2 | clasts | 47°34'10.85"N | 15°11'35.97"E | -4,10 | 3,00 |
| | R12 K1 | clasts | 47°34'10.85"N | 15°11'35.97"E | -3,49 | 3,45 |
| | R13 K1 | clasts | 47°34'10.02"N | 15°11'35.95"E | -3,49 | 2,95 |
| | R13 K2 | clasts | 47°34'10.02"N | 15°11'35.95"E | -4,84 | 3,16 |
| | R14 K1 | clasts | 47°34'10.62"N | 15°11'35.91"E | -3,13 | 3,63 |
| | R14 K4 | clasts | 47°34'10.62"N | 15°11'35.91"E | -2,89 | 4,29 |
| | R14 K5 | clasts | 47°34'10.85"N | 15°11'35.97"E | -3,19 | 3,98 |
| | R19 K5 | clasts | 47°34'10.09"N | 15°11'36.07"E | -2,44 | 3,63 |
| | R14 Z1 | matrix | 47°34'10.62"N | 15°11'35.91"E | -3,68 | 3,00 |
| | R14 Z2 | matrix | 47°34'10.62"N | 15°11'35.91"E | -2,55 | 3,64 |
| | R10 Z1 | matrix | 47°34'11.03"N | 15°11'35.81"E | -2,24 | 2,92 |
| | R19 Z1 | matrix | 47°34'10.09"N | 15°11'36.07"E | -3,00 | 3,97 |
| | R9a M1.1 | calcite cem. | 47°34'11.16"N | 15°11'35.91"E | -2,93 | 2,63 |
| | R16 M1.4 | calcite cem. | 47°34'10.58"N | 15°11'36.00"E | -3,48 | 2,77 |
| | R9a M1.2 | calcite cem. | 47°34'11.16"N | 15°11'35.91"E | -2,36 | 3,14 |

from -1.96 to 3.46 ‰. However, matrix/cement samples plot in a wider field of stable isotope composition (Fig. 12 b) (Tab. 1).

All types of samples from site Fölz plot in a narrow band of δ¹³C values from 2.63 to 4.29 ‰. Variations in δ¹⁸O values range from -4.84 to -1.31 ‰. Dolomite host rock material plots in a δ¹⁸O range from -2,38 to -1,34 ‰. Cataclasite components show lower δ¹⁸O values with respect to host rocks and range from -4,84 to -2,44 ‰. Comminuted matrix matter plots in a δ¹⁸O field similar to clast components from -3,68 to 2,24 ‰.

Calcite cement and vein fillings show similar δ¹⁸O values with respect to matrix material but tend towards lower δ¹³C values from 2,63 to 3,14 ‰ (Fig. 12 c) (Tab. 1).

Host rock data (both δ¹³C and δ¹⁸O) are in the range typical for the Lower Triassic. The trend with enrichment of light isotopes in both systems may be explained by (1) formation of clay minerals that incorporate lighter isotopes, (2) heating of carbon and/or (3) infiltration of meteoric fluid. All these processes may lead to the observed trend, we favour, however, however, situations 1 and 3 that are compatible with the chemical data presented above.

## 6. Discussion

### 6.1 Fault development and comminution

Macroscopic structural investigations on brittle fault zones in the study areas have identified multiple deformation events. Wide cataclastic shear zones (with cataclastic fault cores) mainly develop in the direction of planes of maximum shear stress. The thicknesses of fault cores, between these planes of maximum shear stress concentration, reflect the main amount of displacement along the shear zone. The evolution of cataclastic fault cores is depending on orientation with respect to principal stress axis as well as pre-existing and predominant structures. (Hausegger and Kurz, 2013). The structural evolution is decisive for potential fluid flow, subsequent chemical alterations and fluid-rock interactions (e.g. Crampin, 1999; Conti et al., 2001; Cello et al., 2001b; Billi et al., 2007).

Microstructures document comminution processes that allowed further chemical alteration of fault rocks (Fig. 5 a-c; 7 a-c; 13). Rotation of cataclasite fragments additionally contributed to comminution. Comminution resulted in formation of a fine grained matrix of mainly dolomite (Fig 5 a; 7 a).

All samples show distinct evidence of dedolomitization processes (Ayora et al., 1998; Arenas et al., 1999; Zeeh et al., 2000; Nader et al., 2003; Benito et al., 2006; Arienzo, 2008; Fu et al., 2008; Rameil, 2008) with variable characte-ristics (Fig. 14, 15, 16).
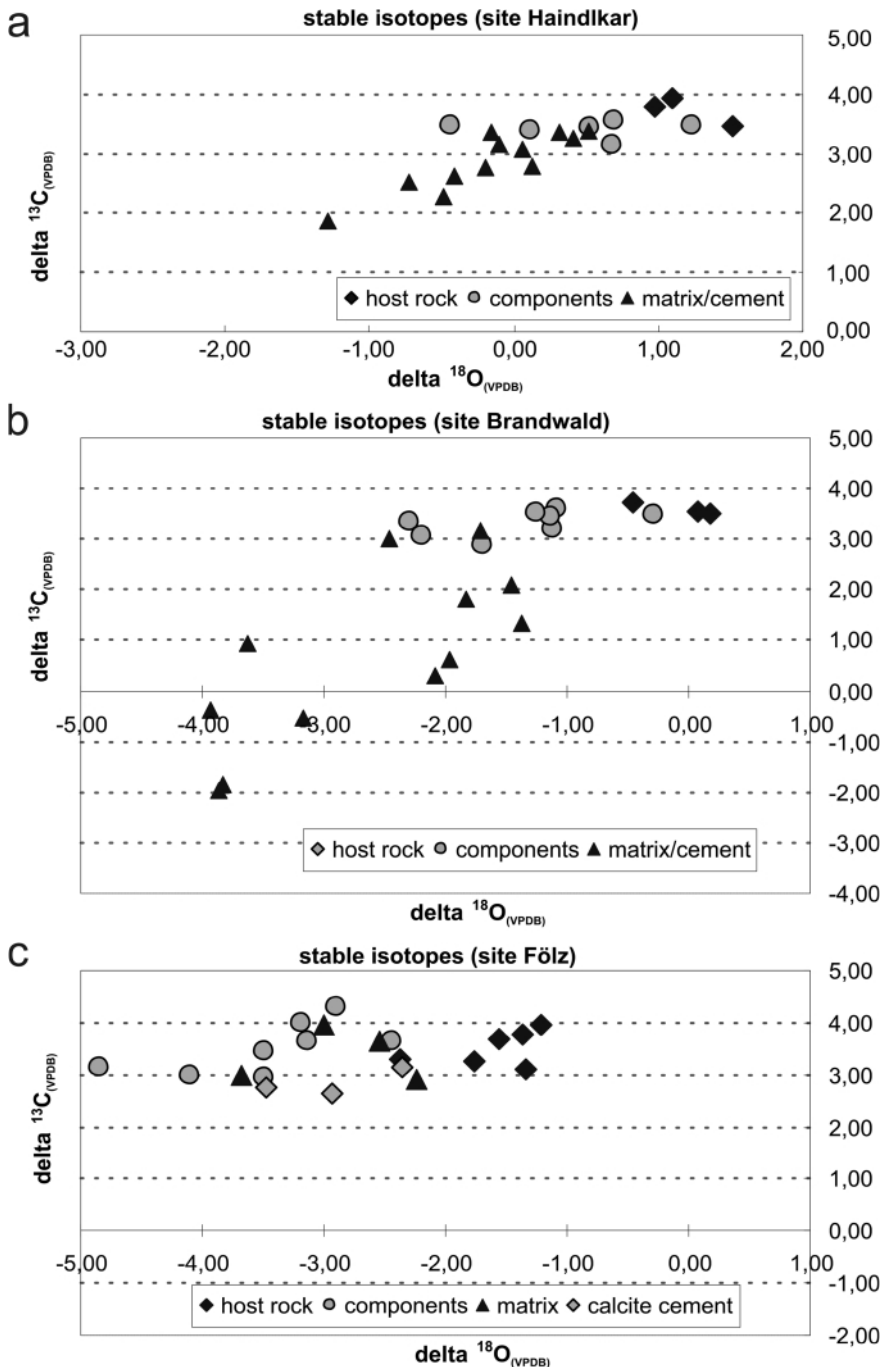


**FIGURE 12:** Stable isotope compositions (δ¹³C and δ¹⁸O in ‰) of host rock slices as well as cataclasite clasts, cataclasite matrix and secondary calcite cement from fault core samples from (a) site Haindlkar, (b) site Brandwald and (c) site Fölz. All sites indicate the tendency of decreased δ¹⁸O values in the course of evolution from host rock to cataclasite components and matrix/cement. (a, b) Dedolomitisised matrix material from site Haindlkar and Brandwald show decreased δ¹³C values.

The most common feature is an increased luminescence along crystal borders and intragranular fractures caused by the dedolomitization along fragment borders. This reaction produces Mg-depleted, Ca-enriched rims around dolomite components and is responsible for observed luminescence behavior (Fig. 4 c, f; 6 c, f; 8 c, f, i; 13 a).

Ultracataclasites are characterized by an advanced stage of dedolomitization (Fig. 13) due to syn- or post-deformational alteration of the fault rock. Due to high displacement (shear) and appropriate fluid chemistry (Ca-rich) and fluid flow, these fault rocks mainly consist of micritic calcite cement/matrix and dolomite components with particle sizes less than 50 μm (Fig. 13b).

## 6.2 Fluid source and fluid flow

Stable isotope composition of $\delta^{13}$C and $\delta^{18}$O was used to get additional information on fluid sources and fluid flow (e.g. Kerrich, 1986; Taylor and Bucher-Nurminen, 1986; Marquer and Burkhard, 1992; Ghisetti et al., 2001; Abart et al., 2002; Pili et al., 2002; Rasser and Fenninger, 2002; Caja et al., 2003; Kopf et al., 2003; Dallai et al., 2005). All samples show variable $\delta^{18}$O values, ranging from -4,84 to 1,49 ‰. Host rock samples exhibit the tendency to higher values than cataclasite components, matrix material and calcite cement (Fig. 12). Host rock and cataclasite components show only slight variation in $\delta^{13}$C values at all three sites, ranging from 2,77 to 4,29 ‰. Samples of matrix material from site Haindlkar and especially from site Brandwald show the tendency to decreased $\delta^{13}$C values of 1.96 to 3,97 ‰, whereas all samples from site Fölz show constant $\delta^{13}$C values between 2,63 to 4,29 ‰ (Fig. 12).

Variation of stable isotope signatures are regarded as related to the amount and the chemical composition of fluids (e.g. Pili et al., 2002; Agosta and Kirschner, 2003). Variations in $\delta^{18}$O values with relative constant $\delta^{13}$C signatures are interpreted as either having derived from meteoric (aqueous) fluids with very little carbon content (e.g. Kerrich, 1986; Ghisetti et al., 2001; Pili et al., 2002; Rasser and Fenninger, 2002) or as repeated infiltration of fluids with variable chemistry (Janssen et al., 1998).

Depletion of $\delta^{13}$C in matrix material at site Brandwald and Haindlkar also indicates a meteoric fluid source. The development to lower $\delta^{13}$C values, with respect to host rock and components, is related to the content of biogenic carbonate and the amount of fluid, penetrating the fault core. High fluid flow prevents equilibration of fluids and solids and causes variations in isotope signatures. Low variation in $\delta^{13}$C signature at site Fölz represents a closed system (e.g. Kirschner and Kennedy, 2001; Pilil et al., 2002; Agosta and Kirschner, 2003).

The development of isotopic signatures from host rocks to components and further matrix material, indicated by decreasing $\delta^{18}$O values and decreasing (site Haindlkar and Brand-
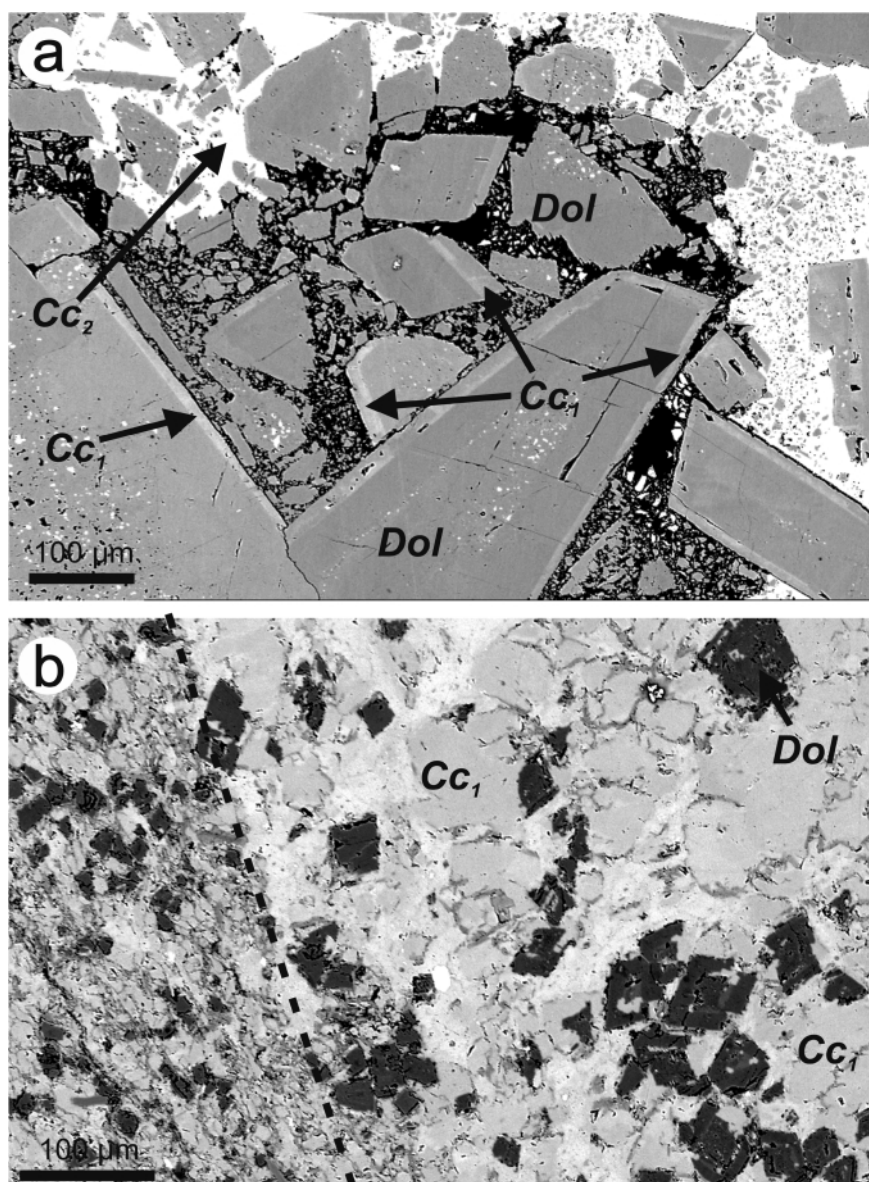


**Figure 13:** BSE images to illustrate dedolomitization and comminution processes. (a) Sample H4 from site Haindlkar consists of dolomite clasts ('Dol'; dark grey) which show brighter rims along crystal borders as result of dedolomitization processes ('Cc₁'). Subsequent cementation with calcite material is illustrated in light grey to white ('Cc₂'). (b) Ultracataclasite sample from site Fölz (sample EA1) showing dolomite clasts with maximum diameters of 50 μm embedded in completely dedolomitizised (calcite) cement ('Cc₁'). Dashed line borders two domains of ultracataclasite in this sample. Left domain exhibits dolomite components with maximum diameters of 20 μm, indicating increased shear and comminution with respect to right domain.

wald) or constant δ¹³C values (site Fölz) (Fig. 12), indicate meteoric derived fluids and low temperatures between 30 and 100°C (e.g. Kerrich, 1986; Agosta and Kirschner, 2003; Nader et al., 2003).

Precipitation of Fe-hydroxides and Fe-bearing carbonates (Phase P2 and P4) indicates that related fluids circulated through deeper parts of the sedimentary sequence. Fe-content is assumed to be derived from clastics, therefore, the underlying Werfen Formation is presumed to be the source for the Fe. Site Fölz is situated in close range to the clastic Werfen Formation and shows Fe-contents up to 10 times higher than samples from site Haindlkar and Fölz. Si-bearing fluids (Phase P2, site Fölz) also reference the Werfen Formation as potential fluid source. Increase in Fe and/or Si is assumend to be an indicator for changing fluid temperature and/or changing pH-value.

## 7. Conclusions

The methodical combination of cathodoluminescence, microprobe- and stable isotope analysis in this study enables the determination, characterization and chronological sequence of different fluid precipitation phases in fault core rocks of brittle fault zones in the Northern Calcareous Alps. The following general assumptions can be deduced from the interpretation of this study's results:

1) From the chemical and CL data five precipitation phases and related processes can be reconstructed and classified with respect to fluid chemistry, CL behavior and structural processes.

2) Besides differentiation of fluid generations, detailed CL images provide an indication of internal, chemical zonation of carbonate vein and pore fillings.
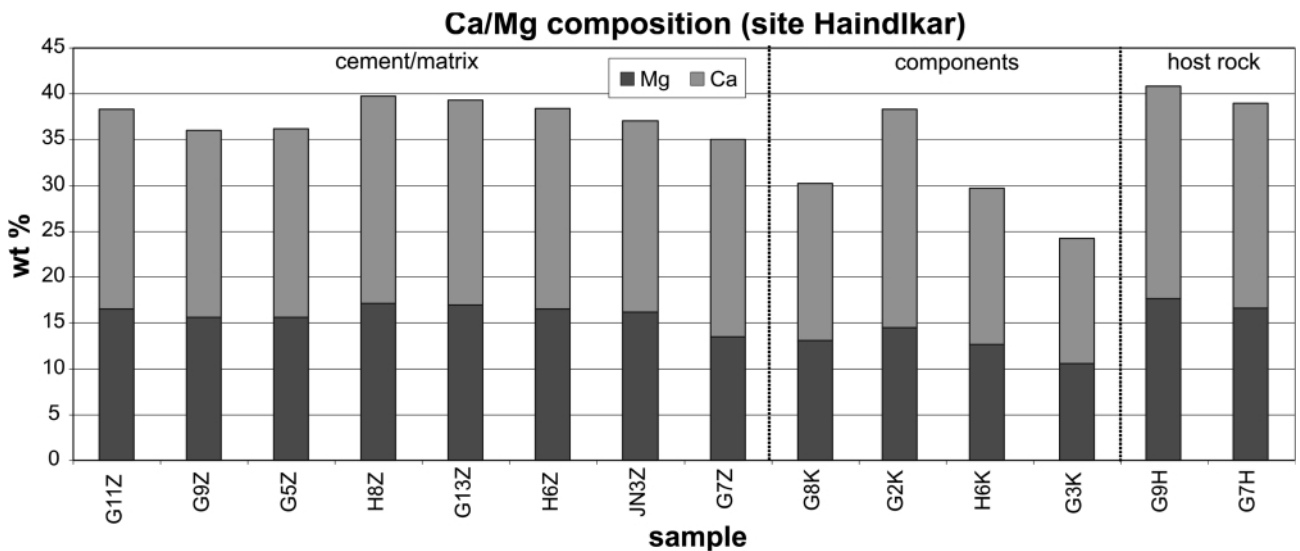


**Figure 14:** Ca and Mg composition of powder samples from site Haindlkar. Though CL and microprobe analysis give distinct evidence for de-dolomitization processes, no significant change in Ca/Mg ratios between host rock, cataclasite components and cement/matrix is visible. Host rock samples may already underwent de-dolomitization in similar extent with respect to cataclasite clasts and matrix.
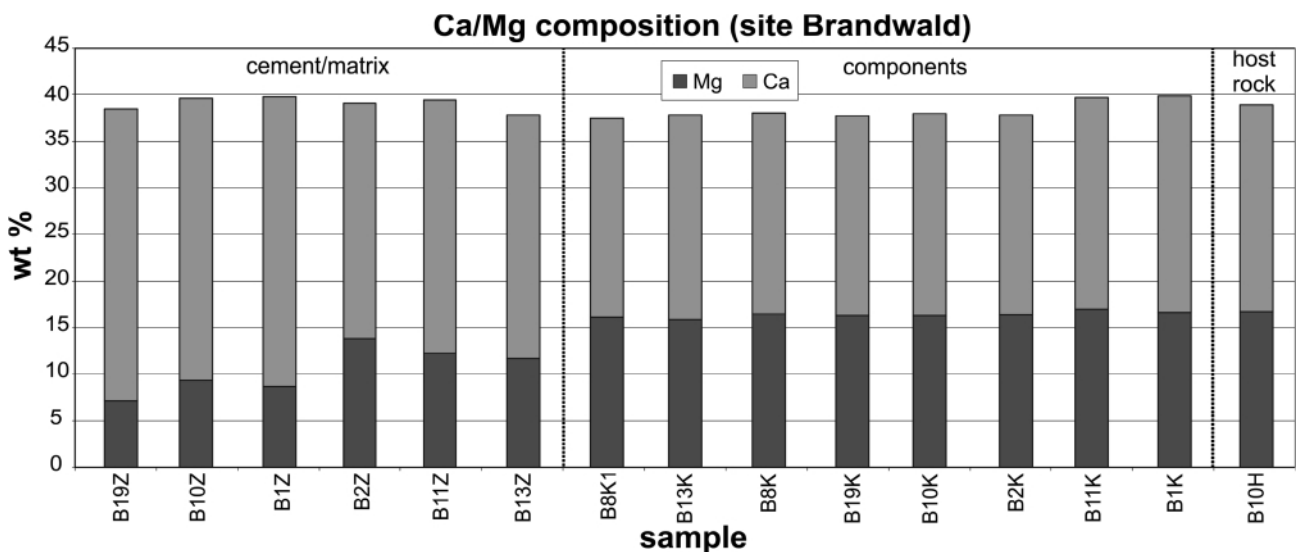


**Figure 15:** Ca and Mg composition of powder samples from site Brandwald. While the Ca/Mg ratio is constant in host rock and cataclasite clasts, matrix samples exhibit distinct indications for de-dolomitization, illustrated by a distinct change of Ca/Mg ratio (decreased Mg- and increased Ca content).
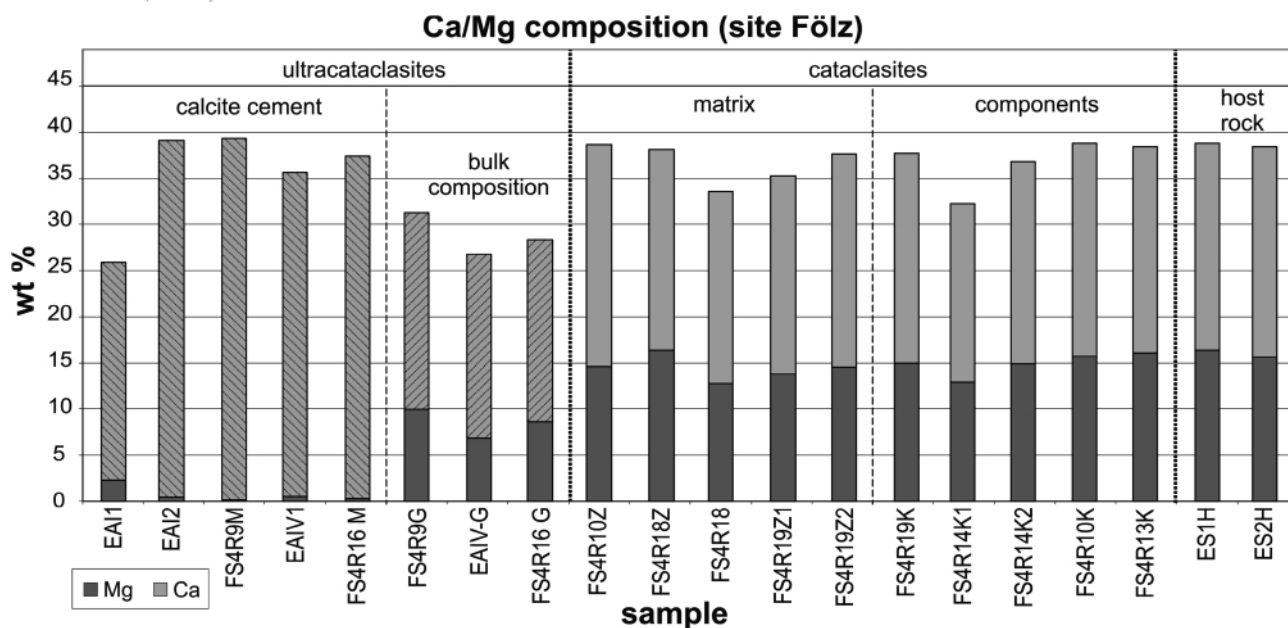
**FIGURE 16:** Ca and Mg composition of powder samples from site Fölz. Ca/Mg ratios of host rock and cataclasite samples exhibit only slight variations. However, ultracataclasite matrix show very low Mg contents and indicate distinct evidence of almost complete de-dolomitization of matrix material into calcite.

3) Stable isotope composition ($\delta^{13}C$ and $\delta^{18}O$) indicates fluid sources of mainly meteoric origin. The extent of variation of isotopic signatures is related to the amount fluid and fluid flow through the fault zone, respectively.

4) Circulation of meteoric derived fluids through deeper, clastic sequences (Werfen Formation) is deduced as potential source for Fe- and Si-contents within the fluids and related precipitation of Fe-hydroxides, Fe-bearing carbonates and quartz vein fillings.

**REFERENCES**

Abart, R., Badertscher, N., Burkhard, M. and Povoden, E., 2002. Oxygen, carbon and strontium isotope systematics in two profiles across the Glarus Thrust: implications for fluid flow. Contributions to Mineralogy and Petrology, 143, 192-208. http://dx.doi.org/10.1007/s00410-001-0326-5

Agosta, F. and Kirschner, D. L., 2003. Fluid conduits in carbonate-hosted seismogenic normal faults of central Italy. Journal of Geophysical Research, 108, 2221-2234. http://dx.doi.org/10.1029/2002JB002013

Arenas, C. and Alonso Zarza, A.M., 1999. Dedolomitization and other ealy diagenetic processes in Miocene lacrustine deposits, Ebro Basin (Spain). Sedimentary Geology, 125, 191-214.

Arienzo, M., 2008. Dedolomitization of the Cambrian Ledger and Kinzers Formations, York County, PA. Franklin & Marshall College, Department of Geosciences, Abstract.

Ayora, C., Taberer, C., Saaltink, M.W. and Carrera, J., 1998. The genesis of dedolomites: a discusion based on reactive transport modeling. Journal of Hydrology, 209, 346-365.

Barker Shaun, L. L., Cox, S.F., Eggins, S.M. and Gagan, M.K., 2006. Microchemical evidence for episodic growth of antiaxial veins during fracture-controlled fluid flow. Earth and Planetary Science Letters, 250, 331-344. http://dx.doi.org/10.1016/j.epsl.2006.07.051

Bauer, F.K., 1998. Zur Frage der Mürzalpendecke im Gebiet der Gesäuseberge und eine Diskussion über die Stellung der Nördlichen Kalkalpen. Jahrbuch der Geologischen Bundesanstalt, 141, 5 - 19.

Bellot, J.-P., 2007. Extensional deformation assisted by mineralised fluids within the brittle-ductile transition: Insights from the southwestern Massif Central, France. Journal of Structural Geology, 29, Issue 2, 225-240.

Benito, M., Lohmann, K. and Mas, R., 2006. Micro-sized dolomite inclusions in ferroan calcite cements developed during burial diagenesis of Kimmeridgian Reefs, northern Iberian Basin, Spain. Journal of Sedimentary Research, 76, Issue 3-4, 472-482. http://dx.doi.org/10.1016/j.jsg.2006.09.004

Billi, A., Salvini, F. and Storti, F., 2003. The damage zone-fault core transition in carbonate rocks: implications for fault growth, structure and permeability. Journal of Structural Geology, 25, 1779–1794. http://dx.doi.org/10.1016/S0191-8141(03)00037-3

Billi, A., Valle, A., Brilli, M., Faccenna, C. and Funiciello, R., 2007. Fracture-controlled fluid circulation and dissolutional weathering in sinkhole-prone carbonate rocks from central Italy. Journal of Structural Geology, 29, 385-395. http://dx.doi.org/10.1016/j.jsg.2006.09.008

Boggs, S. and Krinsley, D., 2006. Application of Cathodoluminescence Imaging to the Study of Sedimentary Rocks. Cambridge University Press, New York.

Budd, D., Hammes, U. and Ward, B., 2000. Cathodoluminescence in Calcite Cements: New Insights on Pb and Zn Sensitizing, Mn Activation and Fe Quenching at low Trace-Element Concentration. Journal of Sedimentary Research, 70, 217-226.

Bustillo, M., Fort, R. and Ordañez, S., 1992. Genetic implications of trace-element distributions in carbonate and non-carbonate phases of limestones and dolostones from western Cantabria, Spain. Chemical Geology, 97, 273-283.

Caine, J.S., Evans, J.P. and Forster, C.B., 1996. Fault zone architecture and permeabiliy structure. Geology, 24, 1025 - 1028.

Caine, J.S. and Foster, C.B., 1999. Fault zone architecture and fluid flow: insights from field data and numerical modelling. In: Haneberg, W. C., Mozley, P.S., Moore, J.C.,Goodwin, L.B. (eds.) - Faults and Subsurface Fluid Flow in the Shallow Crust. Geophysical Monograph, 113, American Geophysical Union, 101–127. http://dx.doi.org/10.1029/GM113p0101

Caja, A.M., Al-Aasm, I.S., Marfil, R., Tsige, M., Martin-Crespo, T. and Salas, R., 2003. Multiphase carbonate cementation related to fractures in the upper Jurassic limestones, Maestrat Basin (Iberian Range, Spain). Journal of Geochemical Exploration, 78/79, 33-38. http://dx.doi.org/10.1016/S0375-6742(03)00045-1

Cello, G., Invernizzi, C., Mazzoli, S., Tondi, E. and 2001a. Fault properties and fluid flow patterns from Quaternary faults in Apennines, Italy. Tectonophysics, 336, 63 – 78. http://dx.doi.org/10.1016/S0040-1951(01)00094-4

Cello, G., Tondi, E., Micarelli, L., Inve, C., and 2001b. Fault zone fabrics and geofluid properties as indicators of rock deformation modes. Journal of Geodynamics, 32, 543–565. http://dx.doi.org/10.1016/S0264-3707(01)00047-3

Conti, A., Turpin, L., Polino, R., Mattei, M., Zuppi, G.M., 2001. The relationship between evolution of fluid chemistry and the style of brittle deformation: examples from the Northern Apennines (Italy). Tectonophysics 330, 103-117.

Crampin, S., 1999. Calculable fluid-rock interactions. Journal of the Geological Society, 156, 501-514.

Dallai, L., Magro, G., Petrucci, E. and Ruggieri, G., 2005. Stable Isotope and noble gas isotope compositions of inclusions fluids from Larderello geothermal field (Italy): Constraints to fluid origin and mixing processes. Journal of Volcanology and Geothermal Research, 148, 152-164. http://dx.doi.org/10.1016/j.jvolgeores.2005.03.019

Decker, K., 2002. Tektonisch/Strukturgeologische Grundlagen, in: Mandl, G. (Ed.), Erstellung moderner geologischer Karten als Grundlage für karstgeologische Spezialuntersuchungen im Hochschwabgebiet. Geologische Bundesanstalt, Vienna.

Decker, K., Meschede, M. and Ring, U., 1993. Fault slip analysis along the northern margin of the Eastern Alps (Molasse, Helvetic nappes, North and South Penninic flysch, and the Northern Calcareous Alps). Tectonophysics, 223, 291-312.

Decker, K., Peresson, H. and Faupl, P., 1994. Die miozäne Tektonik der östlichen Kalkalpen, Kinematik, Paläospannungen und Deformationsaufteilung während der "lateralen Extrusion" der Zentralalpen. Jahrbuch der Geologischen Bundesanstalt 137, 5-18.

Decker, K. and Peresson, H., 1996. Tertiary kinematics in the Alpine–Carpathian–Pannonian system: links between thrusting, transform faulting and crustal extension. In: Wessely, G., Liebl, W. (eds.), Oil and Gas in Alpidic Thrustbelts and Basins of Central and Eastern Europe. EAGE Special Publication, 69–77.

Dietzel, M., Tang, J., Leis, A. and Köhler, S.J., 2009. Oxygen isotopic fractionation during inorganic calcite precipitation — Effects of temperature, precipitation rate and pH. Chemical Geology, 268, 107–115. http://dx.doi.org/10.1016/j.chemgeo.2009.07.015

Faulkner, D.R., Jackson, C.A.L., Lunn, R.J., Schlische, R.W., Shipton, Z.K., Wibberley, C.A.J. and Withjack, M.O., 2010. A review of recent developments concerning the structure, mechanics and fluid flow properties of fault zones. Journal of Structural Geology, 32, 1557-1575. http://dx.doi.org/10.1016/j.jsg.2010.06.009

Fitz-Diaz, E., Hudleston, P., Siebenhaller, L., Kirschner, D., Camprubí, A., Tolson, G., and Pi Puig, T., 2011. Insights into fluid flow and water-rock interaction during deformation of carbonate sequences in the Mexican fold-thrust belt. Journal of Structural Geology, 33, 1237-1253. http://dx.doi.org/10.1016/j.jsg.2011.05.009

Frisch, W., Dunkl, I. and Kuhlemann, J., 2000. Post-collisional orogen-parallel large-scale extension in the Eastern Alps. Tectonophysics 327, 239-265. http://dx.doi.org/10.1016/S0040-1951(00)00204-3

Frisch, W. and Gawlick, H.-J., 2003. The nappe structure of the central Northern Calcareous Alps and ist disintegration during Miocene tectonic extrusion - a contribution to understanding the orogenic evolution of the Eastern Alps. International Journal of Earth Sciences, 92, 712-727.

Frost, E., Dolan, J., Sammis, C., Hacker, B., Cole, J. and Ratschbacher, L., 2009. Progressive strain localization in a major strike-slip fault exhumed from midseismogenic depths: Structural observations from the Salzach-Ennstal- Mariazell-Puchberg fault system, Austria. Journal of Geophysical Research 114, 1-14. http://dx.doi.org/10.1029/2008JB005763

Fu, Q., Qing, H., Bergman, K.M. and Yang, C., 2008. Dedolomitization and calcite cementation in Middle Devonian Winnipegosis Formation in Central Saskatchewan, Canada. Sedimentology, 55, 1623-1642. http://dx.doi.org/10.1111/j.1365-3091.2008.00960.x

Gabrielov, A.M., Keilis Borok, V.I., Pinsky, V., Podvigina, O.M., Shapira, A., Zheligovsky, V.A., 2007. Fluids migration and dynamics of a blocks-and-faults system. Tectonophysics 429, 229-251. http://dx.doi.org/10.1016/j.tecto.2006.09.011

Ghisetti, F., Kirschner, D., Vezzani, L. and Agosta, F., 2001. Stable isotope evidence for contrasting paleofluid circulation in thrust faults and normal faults of central Appennines, Italy. Journal of Geophysical Research, 106, 2221-2234.

Gillhaus, A., Habermann, D., Meijer, J. and Richter, D.K., 2000. Cathodoluminescence spectroscopy and micro-PIXE: combined high resolution Mn-analyses in dolomites - First results. Nuclear Instruments and Methods in Physics Research Section B: Beam Interactions with Materials and Atoms, 161, 842-845.

Götz, J., 2002. Kathodolumineszenz-Mikroskopie und -Spektroskopie in den Geo- und Materialwissenschaften. Mitteilungen der Österreichischen Mineralogischen Gesellschaft, 147.

Habermann, D., Neuser, R. and Richter, D.K., 1996. REE-activated cathodoluminescence of calcite and dolomite: high-resolution spectrometric analysis af CL emission (HRS-CL). Sedimentary Geology, 101, 1-7.

Hausegger, S. and Kurz, W., 2013. Cataclastic faults along the SEMP fault system (Eastern Alps, Austria) – a contribution to fault zone evolution, internal structure and palaeo-stresses. Tectonophysics, 608, 237 - 251. http://dx.doi.org/10.1016/j.tecto.2013.09.032

Hausegger, S., Kurz, W., Rabitsch, R., Kiechl, E. and Brosch, F.J., 2010. Analysis of the internal structure of a carbonate damage zone: Implications for the mechanisms of fault breccia formation and fluid flow. Journal of Structural Geology, 32, 1349-1362. http://dx.doi.org/10.1016/j.jsg.2009.04.014

Hou, X. and Jones, B. T., 2000. Inductively Coupled Plasma/Optical Emission Specroscopy. In: R.A. Meyers (eds.), Encyclopedia of Analytical Chemistry. John Wiley & Sons Ltd, Chichester, 9468-9485.

Janssen, C., Laube, N., Bau, M. and Gray, D.R., 1998. Fluid regime in faulting deformation of the Waratah Fault Zone, Australia, as inferred from major and minor element analyses and stable isotopic signatures. Tectonophysics, 294, 109-130.

Kerrich, R., 1986. Fluid infiltration into fault zones: Chemical, isotopic, and mechanical effects. Pure and Applied Geophysics, 124, 225-268.

Kim, Y.-S., Peacock, D.C.P. and Sanderson, D.J., 2004. Fault damage zones. Journal of Structural Geology, 26, 503–517. http://dx.doi.org/10.1016/j.jsg.2003.08.002

Kirschner, D. and Kennedy, L., 2001. Limited syntectonic fluid flow in carbonate-hosted thrust faults of the Front Ranges, Canadian Rockies, inferred from stable isotope data and structures. Journal of Geophysical Research, 106, 8827-8840.

Kopf, A., Behrmann, J., Deyhle, A., Roller, S. and Erlenkeuser, H., 2003. Isotopic evidence (B, C, O) of deep fluid processes in fault rocks from the active Woodlark Basin detachment zone. Earth and Planetary Science Letters, 208, 51-68. http://dx.doi.org/10.1016/S0012-821X(03)00016-5

Lee, M., Martin, R., Trager-Cowan, C. and Edwards, P., 2005. Imaging of cathodoluminescence zoning in calcite by scanning electron microscopy and hyperspectral mapping. Journal of Sedimentary Research, 75, 313-322. http://dx.doi.org/10.2110/jsr.2005.023

Linzer, H.-G., Decker, K., Peresson, H., Dell'Mour, R. and Frisch, W., 2002. Balancing lateral orogenic float of the Eastern Alps. Tectonophysics, 354, 211-237. http://dx.doi.org/10.1016/S0040-1951(02)00337-2

Linzer, H.-G., Moser, F., Nemes, F., Ratschbacher, L. and Sperner, B., 1997. Build-up and dismembering of the eastern Northern Calcareous Alps. Tectonophysics, 272, 97-124.

Linzer, H.-G., Ratschbacher, L. and Frisch, W., 1995. Transpressional collision structures in the upper crust: the foldthrust belt of the Northern Calcareous Alps. Tectonophysics, 242, 41-61.

Mandl, G., 2000. The Alpine sector of the Tethyan shelf - Examples of Triassic to Jurassic sedimentation and deformation from the Northern Calcareous Alps. Mitteilungen der Österreichischen Geologischen Gesellschaft, 92, 61-77.

Marchel, H.G., 2000. Application of Cathodoluminescence to Carbonate Diagenesis. In: Pagel, M., Barbin, V., Blanc, P. and Ohnenstetter, D. (eds.), Cathodoluminescence in Geosciences. Springer, Berlin.

Marfil, R., Caja, M.A., Tsige, M., Al-Aasm, I.S., Martin-Crespo, T. and Salas, R., 2005. Carbonate -cemented stylolites and fractures in the Upper Jurassic limestones of the Eastern Iberian Range, Spain: A record of palaeofluids composition and thermal history. Sedimentary Geology, 178, 237-257. http://dx.doi.org/10.1016/j.sedgeo.2005.05.010

Marquer, D. and Burkhard, M., 1992. Fluid circulation, progressive deformation and mass-transfer processes in the upper crust: the example of basement-cover relationship in the External Crystalline Massifs, Switzerland. Journal of Structural Geology, 14, 1047-1057.

Micarelli, L., Benedicto, A., Invernizzi, C., Saint-Bezar, B., Michelot, J.L. and Vergely, P., 2005. Influence of P/T conditions an the style of normal fault initiation and growth in limestones from the SE-Basin, France. Journal of Structural Geology, 27, 1577-1598. http://dx.doi.org/10.1016/j.jsg.2005.05.004

Montaser, A., 1992. Inductively coupled plasmas in analytical atomic spectrometry. VCH-Verlagsgesellschaft, Weinheim.

Nader, F.H., Swennen, R. and Ottenburgs, R., 2003. Karst-meteoric Dedolomitization in Jurassic Carbonates, Lebanon. Geologica Belgica, 6, 3-23.

Nölte, J., 2002. ICP Emissionsspektrometrie für Praktiker. Wiley-VCH, Weinheim.

Ortner, H., 2003. Local and far far field stress-analysis of brittle deformation in the western part of the Northern Calcareous Alps, Austria. Geol. Paläont. Mitt. Innsbruck 26, 109-136.

Peresson, H. and Decker, K., 1997. Far-field effects of Late Miocene subduction in the Eastern Carpathians: E-W compression and inversion of structures in the Alpine-Carpathian-Pannonian region. Tectonics, 16, 38-56.

Pili, E., Poitrasson, F. and Gratier, J.-P., 2002. Carbon-oxygen isotope and trace element constraints on how fluids percolate faulted limestones from the San Andreas Fault system: partitioning of fluid sources and pathways. Chemical Geology, 190, 231-250. http://dx.doi.org/10.1016/S0009-2541(02)00118-3

Rameil, N., 2008. Early diagenetic dolomitization and dedolomitization of Late Jurassic and earliest Cretaceous platform carbonates: A case study from the Jura Mountains (NW Switzerland, E France). Sedimentary Geology, 212, 70–85. http://dx.doi.org/10.1016/j.sedgeo.2008.10.004

Rasser, M.W. and Fenninger, A., 2002. Paleoenvironmental and diagenetic implications of d18O and d13C isotope ratios from the Upper Jurassic Plassen limestone (Northern Calcareous Alps, Austria). Geobios, 35, 41-49. http://dx.doi.org/10.1016/S0016-6995(02)00008-6

Ratschbacher, L., Frisch, W., Linzer, H.-G., Merle, O., 1991. Lateral extrusion in the Eastern Alps. Part 2: structural analyses. Tectonics 10, 257–271.

Ratschbacher, L., Frisch, W., Neubauer, F., Schmid, S.M. and Neugebauer, J., 1989. Extension in compressional orogenic belts: the eastern Alps. Geology, 17, 404–407.

Sample, J.C., Reid, M.R., Tobin, H.J. and Moore, J.C., 1993. Carbonate cement indicate channeled fluid flow along a zone of vertical faults at the deformation front of the Cascadia accretionary wedge (northwest U.S. coast). Geology, 21, 507-510.

Schmid, S. M., Fügenschuh, B., Kissling, E. and Schuster, R., 2004. Tectonic map and overall architecture of the Alpine orogen. Eclogae geolicae Helvetiae, 97, 93-117. http://dx.doi.org/10.1007/s00015-004-1113-x

Taylor, B.E. and Bucher-Nurminen, K., 1986. Oxygen and carbon isotope and cation geochemistry of metasomatic carbonates and fluids-Bergell aureole, Northern Italy. Geochimica et Cosmochimica Acta, 50, 1267-1279.

ten Have, T. and Heijnen, W., 1985. Cathodoluminescence activation and zonation in carbonate rocks: an experimental approach. Geologie en Mijnbouw, 64, 297-310.

Todoli, J.-L. and Mermet, J.-M., 2008. Liquid Sample Introduction in ICP Spectrometry. Elsevier, New York.

Wagreich, M. and Decker, K., 2001. Sedimentary tectonics and subsidience modellung of the type Upper Cretaceous Gosua basin (Northern Calcareous Alps, Austria). International Journal for Earth Sciences 90, 714-726. http://dx.doi.org/10.1007/s005310000181

Wang, X. and Neubauer, F., 1998. Orogen-parallel strike-slip faults bordering metamorphic core complexes: the Salzach-Enns fault zone in the Eastern Alps, Austria. Journal of Structural Geology, 20, 799–818.

Zeeh, S., Becker, F., Heggemann, H., 2000. Dedolomitization by meteoric fluids: the Korbach fissure of the Hessian Zechstein basin, Germany. Journal of Geochemical Exploration, 69/70, 173–176.

Stefan HAUSEGGER[1] & Walter KURZ[2)*]

[1] Graz University of Technology, Institute of Applied Geosciences, Member of NAWI Graz#, Rechbauerstrasse 12, A-8010 GRAZ, Austria;

[2] University of Graz, Institute of Earth Sciences, Member of NAWI Graz#, Heinrichstrasse 26, A-8010 GRAZ, Austria;

[*] Corresponding author, walter.kurz@uni-graz.at

## APPENDIX
### Analytical techniques

*Optical microscopy and cathodoluminescence*

Optical microscopy on a petrographic microscope was conducted at the Institute of Applied Geosciences, Graz University of Technology, on a Leica DMLP microscope equipped with an Olympus DP26 digital camera. Digital overview images were recorded in order to locate areas of special interest for subsequent Cathodoluminescence (CL) analysis.

CL microscopy was executed on polished and carbon-coated thin-sections with a Lumic HC5-LM cathodoluminescence microscope at the Department of Lithospheric Research, University of Vienna. The electron beam of this stage is supplied by a heated filament ("hot cathode") delivering true color CL images. Acceleration voltage was fixed at 14 kV, beam current varied from 0,14 to 0,21 mA. Digital high resolution images were recorded  with a high sensitivity CCD Kappa PS 4/40 camera and subsequently processed with common image editing software packages.

Cathodoluminescence (CL) analysis is a powerful tool for the investigation of carbonate rocks and used for visualization of petrographic features which are often  not visible in conventional transmitted-light microscopy (e.g. ten Have and Heijnen 1985; Budd et al. 2000; Habermann et al. 1996; Gillhaus et al. 2000; Götz 2002; Lee et al. 2005; Boggs and Krinsley 2006). CL behavior is generally triggered by the amount and/or ratio of certain elements. The main activation element in carbonates is $Mn^{2+}$, causing orange to red luminescence colors at a minimum concentration of ~20 to 40 ppm. Pairs of REE (e.g., $Eu^{2+}$ and $Eu^{3+}$ or $Tb^{3+}$ and $Dy^{3+}$) can also act as activators and/or influence the colors of $Mn^{2+}$-activated luminescence (e.g. Habermann et al. 1996, Marchel 2000, ten Have and Heijnen, 1985). Main sensitizers for $Mn^{2+}$-activated luminescence in carbonates are $Pb^{2+}$ and $Ce^{3+}$. In natural carbonates $Fe^{2+}$ is considered as the main quencher of $Mn^{2+}$-activated luminescence, being effective from a concentration of ~30 to 35 ppm (Marchel, 2000). In this study CL analysis gives contribution to the understanding and interpretation of diagenesis, deformation history and fluid flow in carbonate fault rocks.

*Microprobe analysis*

Microprobe analysis was an important application for the evolutionary interpretation of investigated fault rocks. Back-scattered electron emission (BSE) images provide an overview of the chemical composition and contribute to the interpretation of brittle deformation and comminution. Element mappings of main (Ca, Mg) and minor (Si, Fe, Mn, Al) elements complete the assembly of analytical micro-scale applications.

Polished and carbon-coated samples were analyzed by electron microprobe analysis (EMPA) using a JEOL JXA8200 at the University of Leoben, Austria. Backscattered electron emission (BSE) images were collected at an accelerating voltage of 15 kV and a beam current of 5 nA. Qualitative single-spot analyses were conducted by energy dispersive X-ray spectrometry (EDS) in order to determine main and accessorial mineral phases using magnifications from 40x (overview) up to 600x for details.

Selected areas were analyzed by wave-length dispersive X-ray spectrometers (WDS) with 600x magnification in order to get element mappings for main (Ca, Mg) and minor elements (Si, Fe, Mn). Analyses were conducted with constant accelerating voltage of 15 kV. Probe current ranged from 50 to 90nA with variable dwell time from 16 to 25 ms in intervals from 0,46 x 0,46 to 2 x 2 μm. The content of each element is stated by the detection level (counts per second), aligned with respect to measurement conditions and evaluated with knowledge from CL and optical microscopy. Hence, element map color levels of images from each site are comparable and support interpretation of micro-structural and geochemical processes.

*Stable isotope analysis*

Stable isotope geochemistry was used in order to determine $\delta^{18}O$ and $\delta^{13}C$ isotopic composition of host rock, cataclasite fragments (components), cataclasite matrix/cement and secondary vein fillings. Discussed and displayed data of 30 different samples were analyzed  at the isotope lab of the Joanneum Research Forschungsgesellschaft mbH (Graz, Austria) using a Gasbench II for automated continuous-flow gas preparation coupled to a Finnigan DELTAplus XP Mass Spectrometer.

Analytical techniques, experimental conditions and data corrections follow the describions in Dietzel et al. (2009) and Hausegger et al. (2010). Sample vessels were cleaned with diluted phosphoric acid, then rinsed three times with deionized water, and dried overnight at 70 °C. 200 to 400 μg of calcite was added to the sample vials, sealed and flushed with He gas to remove residual air from the sample vials. Prior to analyses phosphoric acid was injected into the individual sample vials and reacted with calcite for 82 min at 72.0±0.1 °C. Each sample was analyzed twice (Dietzel et al., 2009). An overall precision of 0.08% for $d^{18}O$ and of 0.06% for $d^{13}C$ has been achieved. Stable isotope results are reported in δ-notation. All δ-values have been normalized into the V-PDB scale.

*Inductively coupled plasma spectrometry (ICP)*

Inductively coupled plasma optical emission spectrometry (ICP-OES), synonym for inductively coupled plasma atomic emission spectroscopy (ICP-AES), is a very common tool in numerous scientific fields e.g. Hou and Jones (2000), Montaser (1992), Nölte (2002), Todoli and Mermet (2008). This analytical technique provides qualitative and quantitative detection of a broad spectrum of elements. ICP-OES analysis was conducted on samples of cement-, matrix-, fragment- and host rock material with a Perkin Elmer Optima 4300 at the Institute of Applied Geosciences, University of Graz. Main elements (Ca, Mg) were detected in order to differentiate calcite and dolomite and to.support the interpretation of deformation and fluid-rock interaction (dedolomitization).